# Quality-controlled meteorological datasets from SIGMA automatic weather stations in northwest Greenland, 2012–2020

Motoshi Nishimura[1*], Teruo Aoki[1], Masashi Niwano[2], Sumito Matoba[3], Tomonori Tanikawa[2], Tetsuhide Yamasaki[4], Satoru Yamaguchi[5], Koji Fujita[6]

[1]National Institute of Polar Research, Tokyo, Japan

[2]Meteorological Research Institute, Japan Meteorological Agency, Ibaraki, Japan

[3]Institute of Low Temperature Science, Hokkaido University, Hokkaido, Japan

[4]Avangnaq Arctic Project, Osaka, Japan

[5]Snow and Ice Research Center, National Research Institute for Earth Science and Disaster Resilience, Niigata, Japan

[6]Graduate School of Environmental Studies, Nagoya University, Nagoya, Japan

*Correspondence to:* Motoshi Nishimura (nishimura.motoshi@nipr.ac.jp)

**Abstract.** In situ meteorological data are essential to better understand ongoing environmental changes in the Arctic. Here, we present a dataset of quality-controlled meteorological observations by two automatic weather stations in northwest Greenland from July 2012 to the end of August 2020. The stations were installed in the~~an~~ accumulation area on the Greenland Ice Sheet (SIGMA-A site, 1490 m a.s.l.) and near the equilibrium line of the Qaanaaq Ice Cap (SIGMA-B site, 944 m a.s.l.). We describe the two-step sequence of quality-control procedures that we used to create increasingly reliable datasets by masking erroneous data records. Those data sets are archived in the Arctic Data archive System (ADS) (SIGMA-A; http://doi.org/10.17592/001.2022041303, SIGMA-B; http://doi.org/10.17592/001.2022041306). We analyzed the resulting 2012–2020 time series of air temperature,~~ positive degree-days,~~ ~~snow height~~surface height, surface albedo, and histograms of longwave radiation (a proxy of cloud formation frequency). We found that ~~snow height~~surface height increased and albedo remained steady at the SIGMA-A site, whereas high air temperatures and clear-sky conditions prevailed while ~~snow height~~surface height was significantly lowering and albedo decreased in the summers of 2015, 2019, and 2020 at the SIGMA-B site. Therefore, it appears that these weather conditions led to apparent~~notable~~ ~~snow height~~surface height decrease~~degradation~~ at the SIGMA-B site but not at the SIGMA-A site. We anticipate that this quality-control method and these datasets will aid in climate studies of northwest Greenland as well as contribute to the advancement of broader polar climate studies.

## 1. Introduction

Recent changes of the Greenland Ice Sheet have likely contributed to the global rise in sea level (e.g., IPCC, 2021). These changes include rising air temperature on the ice sheet, the increasing extent of bare and dark ice (Shimada et al., 2016), and the loss of ice mass (Hanna et al., 2013; IMBIE Team, 2020). Many studies have used regional climate models and atmospheric reanalysis data (e.g., Niwano et al., 2018; Fettweis et al., 2020) to reveal major ablation events in Greenland and to reconstruct the long-term past surface mass balance of the Greenland Ice Sheet. In situ meteorological data provide vital information to monitor environmental changes and inform the models that simulate them; howevertherefore, continuous accumulation of measured data will be more valuablethe existing in situ meteorological data are insufficient for these purposes.

Automatic weather observation in Greenland started with GC-Net (Greenland Climate Network; Steffen and Box, 2001), which was established as a network of automatic weather stations (AWS) in Greenland after 1990. This observation network intended to provide long-term observations of climatological and glaciological factors over Greenland. This was followed by the PROMICE (van As et al., 2011; Fausto et al., 2021) led by the Geological Survey of Denmark and Greenland (GEUS) and the K-transect network (van de Wal et al., 2005), led by Utrecht University in the Netherlands, has been deployed. PROMICE is currently operating the largest observation network in Greenland by contracting the maintenance of GC-Net equipment, and K-transect has deployed equipment mainly in the western part of the country and continues to monitor the area closely. Both networks have provided important long-term meteorological data.Some automatic weather station (AWS) networks have been constructed on the Greenland Ice Sheet, including GC-Net (Steffen and Box, 2001) and PROMICE (van As et al., 2011; Fausto et al., 2021), and have provided important long-term meteorological data.

–To contribute to these efforts and to fill a spatial gap, we established two AWS systems in northwest Greenland (Fig. 1), where rapid environmental changes have occurred in recent years (Aoki et al., 2014). Recent studies of this region have documented a drastic mass loss since the mid-2000s (Mouginot et al., 2019), an expansion of the ablation area (Noël et al., 2019), and a hot spot of increasing rainfall (Niwano et al., 2021). The two sites were established in 2012 as a part of the Snow Impurity and Glacial Microbe effects on abrupt warming in the Arctic (SIGMA) Project, which aimed to clarify the dramatic enhancement of melting of the Greenland Ice Sheet induced by snow impurities (e.g., black carbon, mineral dust). The observational data acquired since that time have been used by glaciological (Yamaguchi et al., 2014; Tsutaki et al., 2017; Matoba et al., 2018; Kurosaki et al., 2020), meteorological (Aoki et al., 2014; Tanikawa et al., 2014; Niwano et al., 2015; Hirose et al., 2021), and biological studies (Onuma et al., 2018; Takeuchi et al., 2018). These data are also valuable because they support the output ofanalytical values of various numerical models (e.g., Niwano et al., 2018; Fujita et al., 2021) and form the basis for robust analytical results.

The datasets from AWS generally contain erroneous data records that are attributed to "Zero

Offset" (Behrens, 2021)sensor noise or natural factors (e.g., riming, ice accretion, snow accumulation on sensors) or "Zero Offset" (Behrens, 2021) for radiation sensors. Various procedures exist for improving the accuracy of such datasets (e.g., Fiebrich et al., 2010; Fausto et al., 2021). In particular, careful Quality Control (QC) procedures, which is a process to improve the quality of data by removing outliers, are required for downward radiation sensors, which are sensitive to solar zenith angle, icing, riming, and snowfall (van den Broeke et al., 2004a, b; Moradi, 2009). Other QC procedures deal with error sources through range, step, and internal consistency tests (Estévez et al., 2011). The specifics of QC methods, for example, the threshold value for detecting erroneous data records, should be adjusted for each observation environment. In this paper, we describe the QC methods used for the in situ meteorological observation data from northwest Greenland, which include existing QC methods, new ones, and combinations of both.

After describing the AWS sites (Sect. 2) and their datasets (Sect. 3), this paper introduces the two separate QC methods used sequentially to mask erroneous data records (Sect. 4). We then present examples of time series of meteorological variables in northwest Greenland, infer their implications for interannual variations in weather conditions, and describe the differences between the two sites (Sect. 5).

## 2. AWSSite general description

The two AWSs are installed at the SIGMA-A site (78.052° N, 67.628° W; 1490 m a.s.l.), on the northwest Greenland Ice Sheet, and the SIGMA-B site (77.518° N, 69.062° W; 944 m a.s.l.), on the Qaanaaq Ice Cap, a peripheral ice cap on the Greenland coast (Fig. 1). They have been in operation since July 2012 (Aoki et al., 2014). The observed parameters and those sensor specifications including abbreviations are listed in Table 1, and the other key constants, variables, and their abbreviations used in this study are also in Table 2.

The SIGMA-A site is 70 km inland from the coast on a ridge of the Greenland Ice Sheet extending northwest from the Greenland Summit; it sits on a flat snow surface with no obstacles around the site (see Fig. 2). This site isIt is considered to be in an accumulation area for the ice sheet (Matoba et al., 2018) based on the analysis of ice-core data (Yamaguchi et al., 2014; Matoba et al., 2017). The SIGMA-B site is 3 km north of the village of Qaanaaq. This site is considered to be located at near the equilibrium lineIts location is supposed to be near the equilibrium line (910 m a.s.l.; Tsutaki et al., 2017) on the Qaanaaq Ice Cap, which ranges in elevation between 30 and 1110 m a.s.l. (Sugiyama et al., 2014). The surface condition at this site varies (see Fig. 2), and significant surface height decreasingsurface melting has occurred in warm years (e.g., Aoki et al., 2014). The site is on a southwest-facing slope (azimuth 220°) with an angle of 4° according to 10 m DEM data (Porter et al., 2018).

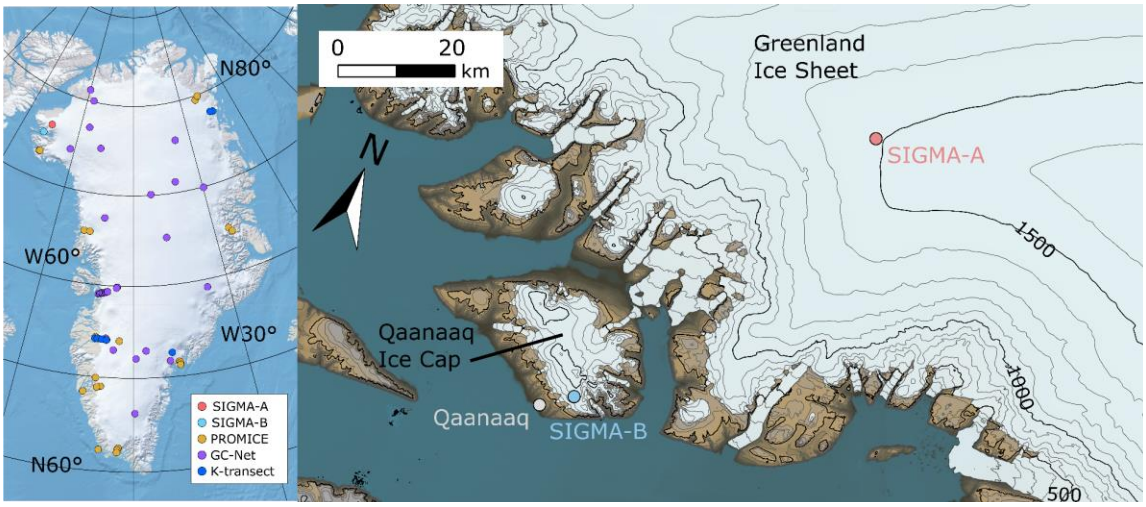


Figure 1. Location map of Greenland showing PROMICE, GC-Net, and K-transect AWS sites (left) and a local map of northwest Greenland showing locations of AWS sites SIGMA-A and SIGMA-B. Contour interval in the right panel is 100 m.

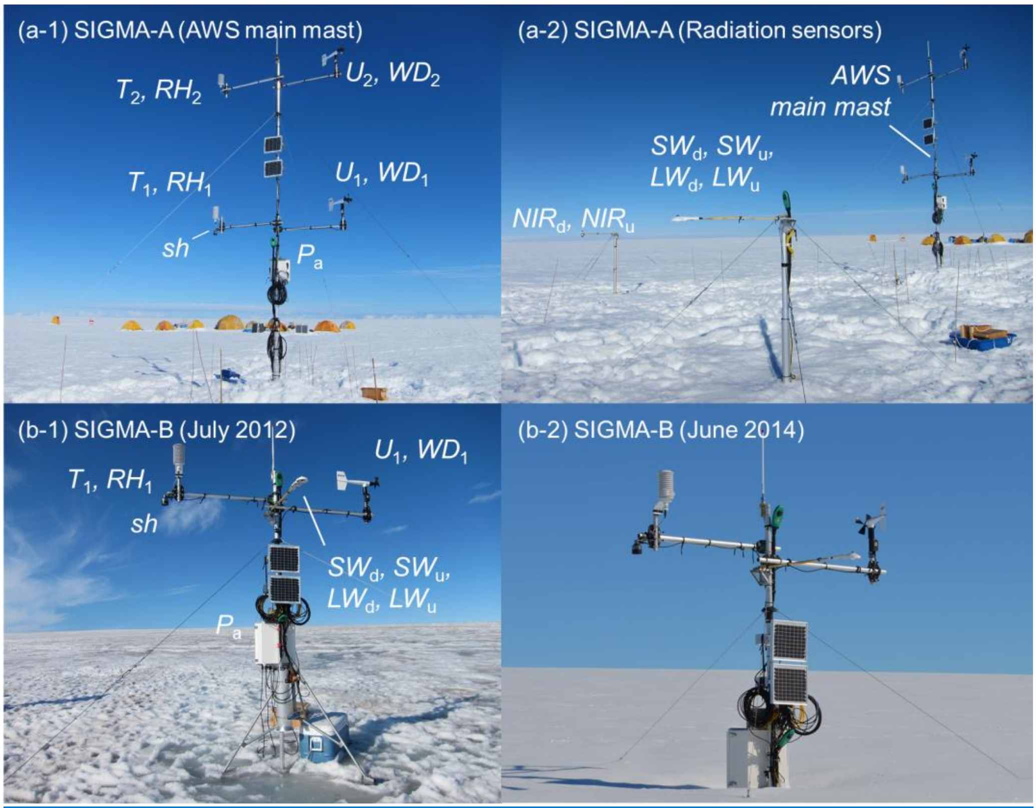

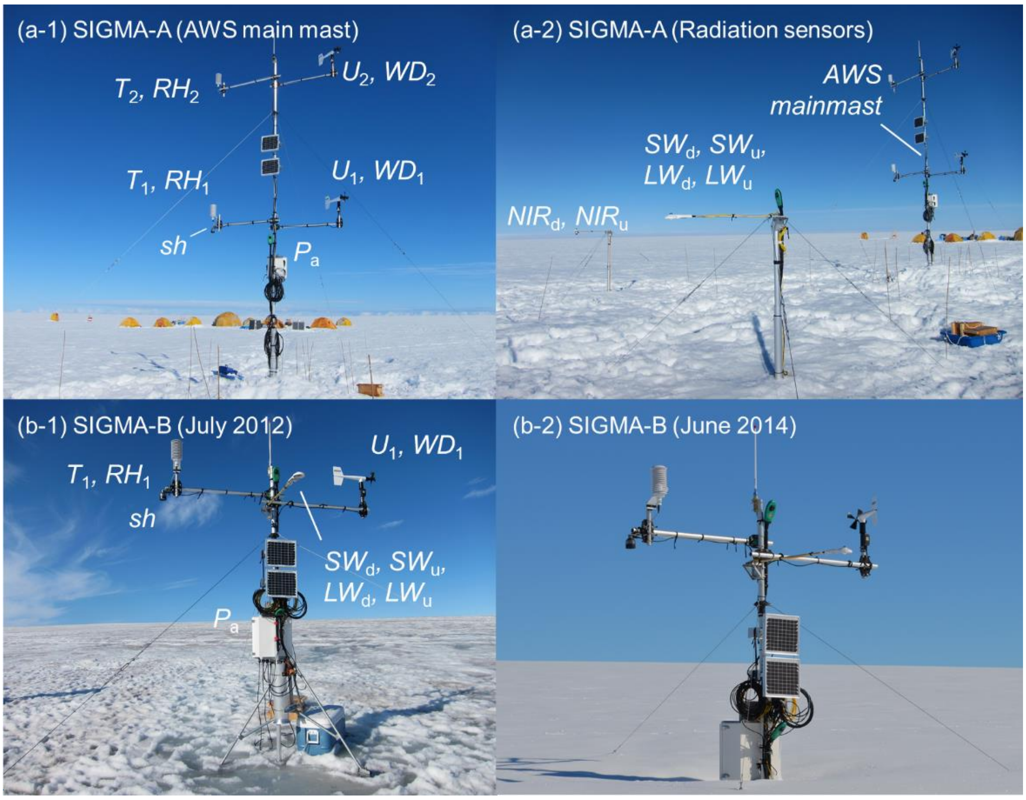


Figure 2. Setting and instrumentation at the SIGMA-A site (top) and the SIGMA-B site (bottom). Surface conditions at SIGMA-B are shown in July 2012 and June 2014. Sensors are labeled with the observation parameters they measure (see Table 1).

Table 1. Meteorological observation parameters and sensor specifications.

| observation parameter | abbreviation | unit | sensor | observaion range | accuracy |
|---|---|---|---|---|---|
| wind speed | $U_n{}^a$ | m s$^{-1}$ | Young, 05103 | 0 to 100 [m s$^{-1}$] | 1.0 m s$^{-1}$ [c] |
| wind direction | $WD_n{}^a$ | degree | Young, 05103 | 360° mechanical,<br>355° electrical (5° open) | 1.1 m s$^{-1}$ at 10° displacement[c] |
| air temperature | $T_n{}^a$ | °C | Vaisala, HMP155[b] | −80 to +60 [°C] | ±0.17 °C |
| relative humidity | $RH_n{}^a$ | % | Vaisala, HMP155[b] | 0 to 100% | ±1% (0 to 90%)<br>±1.7% (90 to 100%) |
| atmospheric pressure | $P_a$ | hPa | Vaisala, PTB210 | 500 to 1100 [hPa] | ±0.30 hPa at 20 °C |
| downward and upward shortwave radiation | $SW_d$, $SW_u$ | W m$^{-2}$ | Kipp & Zonen, CNR4 | 0.3 to 2.8 [μm] | 5 to 20 μV W$^{-1}$ m$^{-2}$ |
| downward and upward longwave radiation | $LW_d$, $LW_u$ | W m$^{-2}$ | Kipp & Zonen, CNR4 | 4.5 to 42 [μm] | 5 to 20 μV W$^{-1}$ m$^{-2}$ |
| downward and upward near-infrared radiation | $NIR_d$, $NIR_u$ | W m$^{-2}$ | Kipp & Zonen, CMP6<br>with a RG715 cut-off filter | 0.715 to 2.8 [μm] | 5 to 20 μV W$^{-1}$ m$^{-2}$ |
| snow height | $sh$ | cm | Campbell, SR50 | 0.5 to 10 [m] | 1 cm or 0.4% |
| snow temperature | $st_n{}^a$ | °C | Climatec, C-PTWP-10 | −40 to +60 [°C] | ±0.15°C |
| tilts of the main mast | $Tilt_X$, $Tilt_Y$ | degree | TURCK, B2N85H-Q20L60- | −85° to +85° | ±0.5° |

a: "n" suffix is appended to distinguish the observation height or depth.
b: protected from direct solar irradiance by a naturally-aspirated 14-plate Gill radiation shield
c: threshold sensitivity

| observation parameter | abbreviation | unit | sensor | observaion range | accuracy |
|---|---|---|---|---|---|
| wind speed | $U_n{}^a$ | m s$^{-1}$ | Young, 05103 | 0 to 100 [m s$^{-1}$] | ± 0.3 m s$^{-1}$ or 1% |
| wind direction | $WD_n{}^a$ | degree | Young, 05103 | 360° mechanical,<br>355° electrical (5° open) | ± 3° |
| air temperature | $T_n{}^a$ | °C | Vaisala, HMP155[b] | −80 to +60 [°C] | ±0.17 °C |
| relative humidity[c] | $RH_n{}^a$ | % | Vaisala, HMP155[b] | 0 to 100% | ±1% (0 to 90%)<br>±1.7% (90 to 100%) |
| atmospheric pressure | $P_a$ | hPa | Vaisala, PTB210 | 500 to 1100 [hPa] | ±0.30 hPa at 20 °C |
| downward and upward shortwave radiation | $SW_d$, $SW_u$ | W m$^{-2}$ | Kipp & Zonen, CNR4 | 0.3 to 2.8 [μm] | ±5% (daily total) |
| downward and upward longwave radiation | $LW_d$, $LW_u$ | W m$^{-2}$ | Kipp & Zonen, CNR4 | 4.5 to 42 [μm] | ±10% (daily total) |
| downward and upward near-infrared radiation | $NIR_d$, $NIR_u$ | W m$^{-2}$ | Kipp & Zonen, CMP6<br>with a RG715 cut-off filter | 0.715 to 2.8 [μm] | ±5% (daily total) |
| surface height | $sh$ | cm | Campbell, SR50 | 0.5 to 10 [m] | 1 cm or 0.4% |
| snow temperature | $st_n{}^a$ | °C | Climatec, C-PTWP-10 | −40 to +60 [°C] | ±0.15°C |
| tilts of the main mast | $Tilt_X$, $Tilt_Y$ | degree | TURCK, B2N85H-Q20L60- | −85° to +85° | ±0.5° |

a: "n" suffix is appended to distinguish the observation height or depth.
b: protected from direct solar irradiance by a naturally-aspirated 14-plate Gill radiation shield
c: Relative humidity is measured relative to water even in sub-freezing environments

Table 2. Key constants, variables, and their symbols used in this paper.

| symbol | name | value | unit |
|---|---|---|---|
| | constant | | |
| $f_{nir}$ | a fraction of near-infrared radiant flux in the shortwave radiant flux at the top of the atmosphere | 0.5151 | no dimension |
| $I_0$ | solar constant | 1361 | W m$^{-2}$ |
| n | cloud cover coefficient | 0.5 | no dimension |
| $r_m$ | annual mean distance between the Sun and the Earth | 1.496×10$^{8}$ | km |
| $sh_{initial}$ | initial height of the surface height sensor | 300 | cm |
| $\alpha_{sw\_max}$ | maximum value of surface albedo | 0.95 | no dimension |
| $\alpha_{nir\_max}$ | maximum value of surface near-infrared albedo | 0.90 | no dimension |
| $\kappa$ | constant depending on cloud type | 0.26 | no dimension |
| $\varepsilon$ | snow/ice surface emissivity | 0.98 | no dimension |
| σ | Stefan-Boltzmann constant | 5.67×10$^{8}$ | W m$^{-2}$ K$^{-4}$ |
| | variable | | |
| d | diffuse fraction in global radiation | | no dimension |
| $I_d$ | diffuse solar radiation | | W m$^{-2}$ |
| $I_s$ | direct solar radiation | | W m$^{-2}$ |
| $LW_d$ | downward longwave radiation | | W m$^{-2}$ |
| $LW_{std}$ | standard atmospheric longwave radiation | | W m$^{-2}$ |
| $LW_u$ | upward longwave radiation | | W m$^{-2}$ |
| $NIR_d$ | downward near-infrared radiation | | W m$^{-2}$ |
| $NIR_u$ | upward near-infrared radiation | | W m$^{-2}$ |
| $P_a$ | atmospheric pressure | | hPa |
| $r$ | distance between the Sun and the Earth | | m |
| $RH_{1,2}$ [a] | relative humidity | | % |
| $sh$ | surface height | | cm |
| $sh_{raw}$ | raw data of surface height | | m |
| $solz$ | solar zenith angle | | degree |
| $solz_{slope}$ | solar zenith angle for a slope | | degree |
| $st_{1\text{-}6}$ [b] | snow temperature | | °C |
| $st\_depth_{1\text{-}6}$ [b] | snow temperature sensor depth | | m |
| $SW_d$ | downward shortwave radiation | | W m$^{-2}$ |
| $SW_{d\_slope}$ | downward shortwave radiation for a slope | | W m$^{-2}$ |
| $SW_{TOA}$ | downward shortwave radiation at the top of the atmosphere | | W m$^{-2}$ |
| $SW_u$ | upward shortwave radiation | | W m$^{-2}$ |
| $t_r$ | transmissivity of the atmosphere for shortwave radiation | | no dimension |
| $T_{1,2}$ [a] | air temperature | | °C |
| $WD_{1,2}$ [a] | wind direction | | degree |
| $U_{1,2}$ [a] | wind speed | | m s$^{-1}$ |
| $\alpha_{sw}$ | surface albedo | | no dimension |
| $\alpha_{sw,i}$ | daily integrated surface albedo | | no dimension |
| $\alpha_{nir}$ | surface near-infrared albedo | | no dimension |
| $\alpha_{nir,i}$ | daily integrated surface near-infrared albedo | | no dimension |
| $\beta$ | slope angle | | radian |
| $\varepsilon_0$ | clear-sky atmospheric emissivity | | no dimension |
| $\varepsilon^*$ | atmospheric emissivity | | no dimension |
| $\theta$ | solar zenith angle | | radian |
| $\theta_{slope}$ | solar zenith angle for a slope | | radian |
| $\phi$ | solar azimuth angle | | radian |
| $\phi_{slope}$ | solar azimuth angle of a slope | | radian |

[a] 1: observed at lower height, 2: observed at upper height (only at the SIGMA-A site)

[b] 1-6: observing depth

## 3. Description of AWS systems and datasets

### 3.1. Specifications

~~Sensor specifications for the meteorological observations are listed in Table 1, and overviews of the two AWS systems are shown in Fig. 2.~~ Each AWS main mast is set in a hole drilled using a hand auger. Sensors for air temperature, relative humidity, and wind speed and direction are mounted at the ends of horizontal poles to exclude possible thermal and wind disturbances from the main mast. The SIGMA-A sensors are placed 3 m and 6 m above the surface, as signified by subscripts "1" (lower) and "2" (upper) in the corresponding data variables. The SIGMA-B sensors are set at 3 m above the surface and have subscripts of "1". The ~~snow height~~surface height sensor at both sites is mounted at 3 m height beneath the air temperature and relative humidity sensors. Six snow temperature sensors have been set as follows. Four sensors were set at 19:00 UTC on 29 June 2012 at depths of 100 cm ($st_1$), ~~0.~~70 cm ($st_2$), ~~0.~~40 cm ($st_3$), and ~~0.0~~5 cm ($st_4$) under the snow surface. At 21:00 UTC on 27 July 2013, sensors $st_3$ and $st_4$ were relocated to depths of ~~0.~~46 cm and ~~0.~~16 cm, respectively. Sensors $st_5$ and $st_6$ were set at ~~0.0~~5 cm under the surface and ~~0.~~45 cm above the surface, respectively, at 14:00 UTC on 9 June 2014. Sensors for shortwave, longwave, and near-infrared radiation are installed at SIGMA-A on separate poles 10 m from the main mast (Fig. 2a-2). A pyranometer and a pyrgeometer at SIGMA-B are mounted on the main mast facing directly south. Tilt angles of the main mast in the north-south ($Tilt_X$) and east-west ($Tilt_Y$) directions are monitored with an inclinometer attached to the main mast. The additional suffix "A" or "B" represents the site name in the variables introduced below.

Electric power is supplied to the AWS systems by a lead-acid~~cyclone~~ battery that is charged constantly by solar panels attached to the ~~mainmast~~main mast. All parameters are recorded once per minute and stored in a data logger (C-CR1000, Campbell Scientific, USA), except for the ~~mainmast~~main mast's ~~snow height~~surface height and tilt angles, which are recorded every hour. Hourly data are calculated for the other parameters by averaging the 1-min data. All hourly data are sent regularly to the data server via the Argos satellite channel.

~~Snow height~~Surface height is measured with an ultrasonic snow gauge (Table 1). The raw data from this sensor ($sh_{raw}$) is the distance from the sensor to the snow surface, which has a temperature dependence. The temperature-corrected ~~snow height~~surface height ($sh$) is calculated from

$$sh = sh_{initial} - sh_{raw} \times \sqrt{\frac{T_2 + 273.15}{273.15}} \times 100, \quad \text{(i)}$$

where $sh_{initial}$ (= 300 cm) is the initially installed sensor height from the surface and $T_2$ is air temperature.

~~Table 1. Meteorological observation parameters and sensor specifications.~~

| observation parameter | abbreviation | unit | sensor | observaion range | accuracy |
|---|---|---|---|---|---|
| wind speed | $U_n$[a] | m s$^{-1}$ | Young, 05103 | 0 to 100 [m s$^{-1}$] | 1.0 m s$^{-1}$ [c] |
| wind direction | $WD_n$[a] | degree | Young, 05103 | 360° mechanical, 355° electrical (5° open) | 1.1 m s$^{-1}$ at 10° displacement[c] |
| air temperature | $T_n$[a] | °C | Vaisala, HMP155[b] | −80 to +60 [°C] | ±0.17 °C |
| relative humidity | $RH_n$[a] | % | Vaisala, HMP155[b] | 0 to 100% | ±1% (0 to 90%) ±1.7% (90 to 100%) |
| atmospheric pressure | $P_a$ | hPa | Vaisala, PTB210 | 500 to 1100 [hPa] | ±0.30 hPa at 20 °C |
| downward and upward shortwave radiation | $SW_d$, $SW_u$ | W m$^{-2}$ | Kipp & Zonen, CNR4 | 0.3 to 2.8 [μm] | 5 to 20 μV W$^{-1}$ m$^{-2}$ |
| downward and upward longwave radiation | $LW_d$, $LW_u$ | W m$^{-2}$ | Kipp & Zonen, CNR4 | 4.5 to 42 [μm] | 5 to 20 μV W$^{-1}$ m$^{-2}$ |
| downward and upward near-infrared radiation | $NIR_d$, $NIR_u$ | W m$^{-2}$ | Kipp & Zonen, CMP6 with a RG715 cut-off filter | 0.715 to 2.8 [μm] | 5 to 20 μV W$^{-1}$ m$^{-2}$ |
| snow height | $sh$ | cm | Campbell, SR50 | 0.5 to 10 [m] | 1 cm or 0.4% |
| snow temperature | $st_n$[a] | °C | Climatec, C-PTWP-10 | −40 to +60 [°C] | ±0.15°C |
| tilts of the main mast | $Tilt_X$, $Tilt_Y$ | degree | TURCK, B2N85H-Q20L60- | −85° to +85° | ±0.5° |

a: "n" suffix is appended to distinguish the observation height or depth.
b: protected from direct solar irradiance by a naturally-aspirated 14-plate Gill radiation shield
c: threshold sensitivity

## 3.2. Data processing

We describe the calculations for some variables used in the QC process in this section.~~Table 2 shows the key constants, variables, and abbreviations used in this study.~~

To accurately calculate the surface albedo and surface energy balance at the SIGMA-B site, we considered the impact of the sloping surface on the vertical radiant flux. To account for this effect, we derived the slope-corrected downward shortwave radiation ($SW_{d\_slope}$) using the methods in Jonsell et al. (2003) and Hock and Holmgren (2005).~~Because the vertical radiant flux against the inclined surface needed to accurately calculate the surface albedo and surface energy balance is affected by the sloping surface at the SIGMA-B site, we calculated the slope-corrected downward shortwave radiation ($SW_{d\_slope}$) from the corresponding observations using the correction method in Jonsell et al. (2003) and Hock and Holmgren (2005).~~ The $SW_{d\_slope}$ is calculated by

$$SW_{d\_slope} = I_s + I_d, \quad \text{(ii)}$$

where $I_s$ and $I_d$ are the direct and diffuse shortwave radiation for a slope, respectively:

$$I_s = SW_d \times d, \quad \text{(iii)}$$

$$I_d = SW_d \times (1 - d) \times \frac{\cos\theta_{slope}}{\cos\theta}, \quad \text{(iv)}$$

where $d$ is the ratio of total diffuse radiation to global radiation and $\theta$ and $\theta_{slope}$ [radian] are the solar zenith angle and the solar zenith angle for a slope, respectively. The ratio $d$ is obtained from atmospheric transmittance $t_r$ by

$$d = \begin{cases} 0.15 & \text{for } 0.8 \leq t_r, \\ 0.929 + 1.134t_r - 5.111{t_r}^2 + 3.106{t_r}^3 & \text{for } 0.15 < t_r < 0.8, \\ 1.0 & \text{for } t_r \leq 0.15, \end{cases} \quad \text{(v)}$$

where

$$t_r = \frac{SW_d}{SW_{\mathrm{TOA}}}, \quad \text{(vi)}$$

where $SW_{\mathrm{TOA}}$ is the downward shortwave radiation at the top of the atmosphere, calculated by

$$SW_{\mathrm{TOA}} = I_0 \left(\frac{r_{\mathrm{m}}}{r}\right)^2 \cos\theta, \quad \text{(vii)}$$

where $I_0$ (= 1361 W m$^{-2}$) is the solar constant (Rottman, 2006; Fröhlich, 2012), $r$ is the distance between the Sun and the Earth (assuming an elliptical orbit with an eccentricity of 0.01637), and $r_{\mathrm{m}}$ is its annual mean (= 1.496 × 10$^8$ km).

The solar zenith angle for a slope in Eq. (iv) is calculated by

$$\cos\theta_{\mathrm{slope}} = \cos\beta\cos\theta + \sin\beta\sin\theta\cos(\varphi - \varphi_{\mathrm{slope}}), \quad \text{(viii)}$$

where $\beta$ is the slope angle from a horizontal plane, and $\varphi$ and $\varphi_{\mathrm{slope}}$ are the solar azimuth and the solar azimuth for the slope direction, respectively. Solar zenith and azimuth angles are calculated from the geographic position of the observation site and the date and time.

Shortwave and near-infrared albedos ($\alpha_{\mathrm{sw}}$ and $\alpha_{\mathrm{nir}}$, respectively) are calculated as the ratio of upward and downward radiant fluxes, as shown for $\alpha_{\mathrm{sw}}$ by

$$\alpha_{\mathrm{sw}} = \frac{SW_{\mathrm{u}}}{SW_{\mathrm{d}}}, \quad \text{(ix)}$$

where $SW_{\mathrm{u}}$ is the upward shortwave radiant flux and $SW_{\mathrm{d}}$ is the downward shortwave radiant flux. The daily integrated shortwave albedo ($\alpha_{\mathrm{sw,i}}$) is calculated as the ratio of cumulative upward and downward radiant fluxes for the past 24 h:

$$\alpha_{\mathrm{sw,i}} = \textstyle\sum_{24\mathrm{h}} SW_{\mathrm{u}} / \sum_{24\mathrm{h}} SW_{\mathrm{d}}. \quad \text{(x)}$$

The near-infrared albedo ($\alpha_{\mathrm{nir}}$) and daily integrated near-infrared albedo ($\alpha_{\mathrm{nir,i}}$) are calculated in the same way. The near-infrared fraction is the ratio of the downward near-infrared radiant flux ($NIR_{\mathrm{d}}$) to $SW_{\mathrm{d}}$.

Note that some parameters may require correction or caution depending on the observation environment. First, since temperature and humidity shelters are naturally ventilated, air temperature value may have a positive bias due to shelter heating from solar radiation (e.g., Morino et al, 2021). In addition, in sub-freezing conditions, relative humidity may not be measured correctly because the sensor used in this study (Vaisala, HMP155) calculates relative humidity as liquid water vapor pressure even in sub-freezing environments and if the shelter is covered by rime or frost (Makkonen and Laakso, 2005). Aoki et al. (2011) pointed out that the pole on which the radiometer is mounted casts a shadow on the radiation sensor, which may result in incorrect radiation measurements.

Although the possibility of data correction as described above is recognized, the focus of this paper is to open the observed values themselves, without any correction or data processing that might involve the implementer's intention. Therefore, we will note only the correction possibilities and present the observed data in this study.

Table 2. Key constants, variables, and their symbols used in this paper.

| symbol | name | value | unit |
|---|---|---|---|
| | constant | | |
| $f_{nir}$ | a fraction of near-infrared radiant flux in the shortwave radiant flux at the top of the atmosphere | 0.5151 | no dimension |
| $I_0$ | solar constant | 1361 | $W\ m^{-2}$ |
| n | cloud cover coefficient | 0.5 | no dimension |
| $r_m$ | annual mean distance between the Sun and the Earth | $1.496 \times 10^8$ | km |
| $sh_{initial}$ | initial height of the snow height sensor | 300 | cm |
| $\kappa$ | constant depending on cloud type | 0.26 | no dimension |
| $\varepsilon$ | snow/ice surface emissivity | 0.98 | no dimension |
| σ | Stefan-Boltzmann constant | $5.67 \times 10^8$ | $W\ m^{-2}\ K^{-4}$ |
| | variable | | |
| d | diffuse fraction in global radiation | | no dimension |
| $I_d$ | diffuse solar radiation | | $W\ m^{-2}$ |
| $I_s$ | direct solar radiation | | $W\ m^{-2}$ |
| $LW_d$ | downward longwave radiation | | $W\ m^{-2}$ |
| $LW_{std}$ | standard atmospheric longwave radiation | | $W\ m^{-2}$ |
| $LW_u$ | upward longwave radiation | | $W\ m^{-2}$ |
| $NIR_d$ | downward near-infrared radiation | | $W\ m^{-2}$ |
| $NIR_u$ | upward near-infrared radiation | | $W\ m^{-2}$ |
| $P_a$ | atmospheric pressure | | hPa |
| $r$ | distance between the Sun and the Earth | | m |
| $RH_{1,2}$ [a] | relative humidity | | % |
| $sh$ | snow height | | cm |
| $sh_{raw}$ | raw data of snow height | | m |
| $solz$ | solar zenith angle | | degree |
| $solz_{slope}$ | solar zenith angle for a slope | | degree |
| $st_{1\text{-}6}$ [b] | snow temperature | | °C |
| $st\_depth_{1\text{-}6}$ [b] | snow temperature sensor depth | | m |
| $SW_d$ | downward shortwave radiation | | $W\ m^{-2}$ |
| $SW_{d\_slope}$ | downward shortwave radiation for a slope | | $W\ m^{-2}$ |
| $SW_{TOA}$ | downward shortwave radiation at the top of the atmosphere | | $W\ m^{-2}$ |
| $SW_u$ | upward shortwave radiation | | $W\ m^{-2}$ |
| $T_r$ | transmissivity of the atmosphere for shortwave radiation | | no dimension |
| $T_{1,2}$ [a] | air temperature | | °C |
| $WD_{1,2}$ [a] | wind direction | | degree |
| $U_{1,2}$ [a] | wind speed | | $m\ s^{-1}$ |
| $\alpha_{sw}$ | surface albedo | | no dimension |
| $\alpha_{sw,i}$ | daily integrated surface albedo | | no dimension |
| $\alpha_{nir}$ | surface near-infrared albedo | | no dimension |
| $\alpha_{nir,i}$ | daily integrated surface near-infrared albedo | | no dimension |
| $\beta$ | slope angle | | radian |
| $\varepsilon_0$ | clear-sky atmospheric emissivity | | no dimension |
| $\varepsilon^*$ | atmospheric emissivity | | no dimension |
| $\theta$ | solar zenith angle | | radian |
| $\theta_{slope}$ | solar zenith angle for a slope | | radian |
| $\phi$ | solar azimuth angle | | radian |
| $\phi_{slope}$ | solar azimuth angle of a slope | | radian |

[a] 1: observed at lower height, 2: observed at upper height (only at the SIGMA-A site)

[b] 1-6: observing depth

## 4. Quality control

The datasets of observations at sites SIGMA-A and SIGMA-B are classified into four QC levels numbered 1.0 to 1.3. A Level 1.0 dataset, which is not archived in any repository, is a raw dataset without data processing. A Level 1.1 dataset is a raw dataset with flags added to indicate missing data for periods when the data logger was inoperative. A Level 1.2 dataset has undergone an initial control, which uses a simple masking algorithm to eliminate anomalous values that violate physical laws or are impossible in the observed environment. The initial control improves the accuracy of the statistical processing that follows and reduces the possibility of excluding true values. A Level 1.3 dataset has undergone a secondary control, in which statistical methods are used on Level 1.2 data to identify and mask outlier values. It has also undergone a final manual masking procedure, in which a researcher visually checks the dataset and masks outliers based on subjective criteria.

The initial control method is described in Sect. 4.1 and the secondary control method is described in Sect. 4.2. In these sections, the parameter suffixes related to the differences in observation height (1 and 2) and sites (A and B) are omitted except when needed for clarity, and subscripts indicating upward and downward radiation (d; downward, u; upward) is denoted as $\chi$ in the equation. Erroneous records are flagged with one of the following numerical expressions to signify the reason they have been flagged:

−9999: a missing or erroneous data record attributed to a mechanical malfunction or a local phenomenon such as sensor icing, riming, or burial in snow.

−9998: an erroneous radiation record when the radiant sensor was covered with snow or frost.

−9997: a record of snow temperature sensor depth when the sensor was suspected to be located above, not below the snow surface.

−8888: a record flagged during the manual masking procedure.

### 4.1. Initial QC for Level 1.2 datasets

The objectives of the initial control are to eliminate erroneous records due to mechanical malfunctions or local phenomena and pre-treat Level 1.1 datasets for the secondary control. The initial control consists of a range test (e.g., Fiebrich et al., 2010; Estévez et al., 2011) and a manual mask procedure. The range test sets variation ranges (see Tables 3 and 4) for each observed parameter in northwest Greenland on the basis of simple statistics (maximum, minimum, and mean values) derived from records in the Level 1.1 dataset during a period with no obvious erroneous data. Records outside this statistical range are flagged with a "−9999" code. Tables 3 and 4 list~~s~~ the parameters subjected to this test and their assigned ranges. The manual masking procedure identified specific erroneous values that resulted from an electrical malfunction and flagged them with a "−8888" code. The following subsections offer detailed and additional explanations of the initial control, however, in the following description, only the procedure numbers in Table 3 are referenced as necessary, and the explanation of the range test is omitted.~~.~~

#### 4.1.1. Wind speed and wind direction

~~The ranges for wind speed ($U_n$) and wind direction ($WD_n$) were set at~~

~~$0 < U_n < U_{max} + 15.0,$ (1.1.1)~~

~~$0 < WD_n \leq 360.$ (1.1.2)~~

$U_{max}$ used in the range test is the maximum value between the beginning of observation and 31 August 2020, and +15.0 m s$^{-1}$ was taken as the range margin for the upper limit of $U_n$. In addition to the range test, the following basic processing was also performed.~~No data points for $U_n$ were flagged by this initial control; however, the secondary control added a further condition that flagged erroneous values.~~

When $U_n$ was zero (no wind), $WD_n$ was flagged as erroneous:

$U_n = 0$ and $WD_n > 0 \rightarrow WD_n$ flagged −9999. (1.1.1~~3~~)

When $WD_n$ had a negative value, it was flagged as erroneous~~modified to zero~~:

$WD_n \leq 0 \rightarrow WD_n$ ~~= 0~~ flagged –9999.

(1.1.2~~4~~)

#### 4.1.2. Air temperature and relative humidity

~~The ranges for air temperature ($T_n$) and relative humidity ($RH_n$) were set at~~

~~$T_{n\_min} - 10.0 < T_n < T_{n\_max} + 10.0,$ (1.2.1)~~

~~$0 \leq RH_n \leq 100.$ (1.2.2)~~

$T_{n\_max}$ and $T_{n\_min}$ were determined from the observation period ending 31 August 2020. The range margin for $T_n$ was set as ±10.0 °C. Discrepancies arising from the dual sensors at SIGMA-A were addressed in the secondary control (see Sect. 4.2.2).

#### 4.1.3. Shortwave and near-infrared radiation

The main objective of the initial control for shortwave radiation was to mask erroneous records attributed to Zero Offset (Behrens, 2021)~~electrical noise~~. Zero Offset is a few watts of radiation that occurs at night caused by the slight temperature difference between the two detectors (inside of the dome shelter and sensor body). However, since the value is an observation error, the observed value may be different from the original radiation balance and need to be masked.

The range test is based on the assumption that $SW_d$ cannot exceed the maximum of $SW_{TOA}$ ($SW_{TOA\_max}$) during the observation period (761.6 W m$^{-2}$ at SIGMA-A and 772.2 W m$^{-2}$ at SIGMA-B), and albedos $a_{sw}$ and $a_{nir}$ cannot be higher~~lower~~ than $a_{sw\_max}$ and $a_{nir\_max}$ ($a_{sw\_max}$ = 0.95 and $a_{nir\_max}$

= 0.90), respectively, as determined from the radiative transfer model calculation (Aoki et al., 2003). Moreover, the fraction of the near-infrared spectral domain at the top of the atmosphere ($f_{nir}$) is assumed to be equal to 0.5151 based on the extraterrestrial spectral solar radiation (Wehrli, 1985). Based on those assumptions, upward and downward radiation fluxes were flagged as erroneous (−9999) according to the range tests in Table 3.following criteria:

$$SW_d >< SW_{TOA\_max} \rightarrow SW_d = -9999, \quad (1.3.1)$$

$$NIR_d >< f_{nir}\, SW_{TOA\_max} \rightarrow NIR_d = -9999, \quad (1.3.2)$$

$$SW_u >< 0.95\, SW_{TOA\_max} \rightarrow SW_u = -9999, \quad (1.3.3)$$

$$NIR_u >< 0.90\, f_{nir}\, SW_{TOA\_max} \rightarrow NIR_u = -9999. \quad (1.3.4)$$

The following procedures were also applied to mask erroneous records due to Zero Offsetelectrical noise. These parameters were flagged as erroneous (−9999) in a following case (using $SW_\chi$ as an example): when

$$(SW_{d\chi}, SW_u, NIR_d, NIR_u) < 0 \text{ and } solz < 90.0 \rightarrow SW_\chi \text{ flagged } -9999, \quad (1.3.14)$$

and were changed to zero when

$$(SW_{d\chi}, SW_u, NIR_d, NIR_u) < 0 \text{ and } solz \geq 90.0 \rightarrow SW_\chi = 0. \quad (1.3.25)$$

#### 4.1.4. Longwave radiation

The range testss were performed for $LW_d$ and $LW_u$ under the conditions in Table 3. $LW_{d\_max}$ and $LW_{u\_max}$ were determined as followswere set as follows:

$$0 < LW_d\ (LW_u) < LW_{d\_max}\ (LW_{u\_max}), \quad (1.4.1)$$

where

$$LW_{d\_max} = \varepsilon_{max} \sigma\, T_{2A\_max}\ (T_{1B\_max}), \quad (1.4.12)$$

$$LW_{u\_max} = \varepsilon \sigma\, T_{s\_max}. \quad (1.4.23)$$

However, $T_{max}$ is $T_{2A\_max}$ for the SIGMA-A site and $T_{1B\_max}$ for the SIGMA-B site. Maximum values were determined under the following assumptions: (1) $T_{2A}$ and $T_{1B}$ cannot be larger than $T_{2A\_max}$ and $T_{1B\_max}$, respectively, (2) atmospheric emissivity is set to unity ($\varepsilon_{max}$), and (3) the value of $LW_{u\_max}$ is determined as the amount of radiation corresponding to longwave emission atby assuming that the surface temperature cannot exceed $T_{s\_max}$ (= 10 °C), which includes errors due to longwave emissions from the poles of the AWS system and similar sources, and that the emissivity of the snow/ice surface

($\varepsilon$) is 0.98 (Armstrong and Brun, 2008).

Both upward and downward longwave fluxes were considered erroneous when the sensor appeared to be covered with snow or frost:

$$|LW_{\mathrm{d}} - LW_{\mathrm{u}}| \leq 1.0 \ \rightarrow \ LW_{\mathrm{d}} \ \text{and} \ LW_{\mathrm{u}} \ \text{flagged} -9998. \qquad (1.4.34)$$

### 4.1.5. ~~Snow height~~Surface height

The range test for ~~snow height~~surface height ($sh$) was imposed separately for each period between maintenances to the SIGMA-A site, when the ~~mainmast~~main mast extension was adjusted to prevent the sensors from being buried in snow. (A single range test sufficed for SIGMA-B.) For each test, the range was set so that $sh$ varied from the median by ±100 cm or ±150 cm, a margin that was determined depending on the variation of the data records in each period. The objective of this range test (Procedure 1.5.1; Table 3) was to mask the most obvious outliers. In addition, corrections were made to the $sh$ records after each of three maintenance visits to the AWS at SIGMA-A.

### 4.1.6. Atmospheric pressure

~~The range test for atmospheric pressure ($P_{\mathrm{a}}$) was conducted according to~~

~~$P_{\mathrm{a\_ave}} - 100.0 < P_{\mathrm{a}} < P_{\mathrm{a\_ave}} + 100.0,$ (1.6.1)~~

~~where~~ $P_{\mathrm{a\_ave}}$ used in the range test is the average atmospheric pressure for the observation period at each AWS site (Table 3). The additional margin that defined the range was ±100 hPa.

### 4.1.7. Snow temperature

The range test for snow temperature was conducted using following threshold values; ~~The range test for snow temperature ($st_{\mathrm{n}}$) was conducted according to~~

~~$T_{1\_\mathrm{min}} < st_{\mathrm{n}} < 0.2,$ (1.7.1)~~

~~where~~ $T_{1\_\mathrm{min}}$ is the minimum air temperature for the site and the upper threshold, 0.2 °C, incorporates the sensor’s absolute error of 0.15 °C and the requirement that the snow temperature cannot be positive.

Table 3. Range test coverage for each parameter used in the QC procedures. The variable subscripts “n” (1 or 2) and χ indicate the distinction of sensors height and the direction of radiation flux (upward or downward), respectively.

| parameter | variable | unit | range test: value range | | | range test: procerdure No. |
|---|---|---|---|---|---|---|
| wind speed | $U_1$, $U_2$ | $m\ s^{-1}$ | 0 < | $U_n$ | < $U_{max}$ + 15.0 | 1.1.3 |
| wind direction[a] | $WD_1$, $WD_2$ | degree | 0 < | $WD_n$ | ≦ 360 | 1.1.4 |
| air temperature | $T_1$, $T_2$ | °C | $T_{n\_min}$ − 10.0 < | $T_n$ | < $T_{n\_max}$ + 10.0 | 1.2.1 |
| relative humidity | $RH_1$, $RH_2$ | % | 0 ≦ | $RH_n$ | ≦ 100 | 1.2.2 |
| shortwave radiation | $SW_d$, $SW_u$ | $W\ m^{-2}$ | | $SW_d$ | < $SW_{TOA\_max}$ | 1.3.3 |
| | | | | $SW_u$ | < $SW_{TOA\_max} \times a_{sw\_max}$ | 1.3.5 |
| | | | | $SW_d$ | < $T_{rA\ (or\ B)} \times SW_{TOA\_max}$ | 2.3.2 |
| near-infrared radiation[b] | $NIR_d$, $NIR_u$ | $W\ m^{-2}$ | | $NIR_d$ | < $f_{nir} \times SW_{TOA\_max}$ | 1.3.4 |
| | | | | $NIR_u$ | < $f_{nir} \times SW_{TOA\_max} \times a_{nir\_max}$ | 1.3.6 |
| | | | | $NIR_d$ | < $T_{rA} \times f_{nir} \times SW_{TOA\_max}$ | 2.3.3 |
| surface albedo | $a_{sw}$ | – | 0.6 < | $a_{sw}$ | < 0.95 (for October–April in SIGMA-A) | 2.4.1 |
| | | | 0.4 < | $a_{sw}$ | < 0.95 (for May–September in SIGMA-A) | 2.4.2 |
| | | | 0.4 < | $a_{sw}$ | < 0.95 (for October–April in SIGMA-B) | 2.4.3 |
| | | | 0.1 < | $a_{sw}$ | < 0.95 (for May–September in SIGMA-B) | 2.4.4 |
| surface near-infrared albedo | $a_{nir}$ | – | 0.5 < | $a_{nir}$ | < 0.90 (for October–April in SIGMA-A) | 2.4.5 |
| | | | 0.3 < | $a_{nir}$ | < 0.90 (for May–September in SIGMA-A) | 2.4.6 |
| longwave radiation | $LW_d$, $LW_u$ | $W\ m^{-2}$ | 0 < | $LW_\chi$ | < $LW_{\chi\_max}$ | 1.4.4 |
| surface height | $sh$ | cm | median_sh − 100.0 or 150.0[c] < | $sh$ | < median_sh + 100.0 or 150.0[c] | 1.5.1 |
| atmospheric pressure | $P_a$ | hPa | $P_{a\_ave}$ − 100.0 < | $P_a$ | < $P_{a\_ave}$ + 100.0 | 1.6.1 |
| snow temperature[b] | $st$ | °C | $T_{1\_min}$ − 10.0 < | $st_n$ | < 0.2 | 1.7.1 |

[a] in case of $U_n > 0$
[b] only SIGMA-A site
[c] the margin is changed depending on a variation of the data record in each applied period.

Table ~~3~~4. Threshold values used in the range tests, determined from the entire observation period up to 31 August 2020.

| meteorological parameter | unit | threshold value: SIGMA-A parameter name | SIGMA-A value | SIGMA-B parameter name | SIGMA-B value |
|---|---|---|---|---|---|
| wind speed | $m\ s^{-1}$ | $U_{1A\_max}$ | 23.9 | $U_{1B\_max}$ | 21.9 |
| | | $U_{2A\_max}$ | 25.5 | – | – |
| air temperature | °C | $T_{1A\_max}$ | 7.2 | $T_{1B\_max}$ | 10.7 |
| | | $T_{2A\_max}$ | 7.2 | – | – |
| | | $T_{1A\_min}$ | −49.9 | $T_{1B\_min}$ | −40.5 |
| | | $T_{2A\_min}$ | −49.9 | – | – |
| longwave radiation | $W\ m^{-2}$ | $LW_{dA\_max}$ | 418.8 | $LW_{dB\_max}$ | 440.1 |
| | | $LW_{uA\_max}$ | 357.2 | $LW_{uB\_max}$ | 357.2 |
| atmospheric pressure | hPa | $P_{a\_aveA}$ | 833.1 | $P_{a\_aveB}$ | 894.2 |

## 4.2. Secondary QC for Level 1.3 datasets

The secondary control applies another range test, an anomaly test, and a manual mask procedure. The range test~~, applied only to the shortwave radiation and albedo data,~~ sets a more precise variation range than the initial control and masks erroneous data records. The anomaly test sets a median and standard deviation (SD), which govern statistical tests as follows;

$$\beta < \text{median\_}\beta + \text{SD\_}\beta \times \gamma, \qquad (2.0.1)$$

where $\beta$ is an arbitrary variable and the multiplier $\gamma$ is 1, 2, or 3 depending on the intensity of the anomaly variation, and determined based on the test results in each case. This study ~~used to~~ determined the possible range of normal values in the Level 1.2 dataset and identify and mask outliers if the variable deviates from its normal range. The manual mask procedure identifies and masks any remaining erroneous records. As a result of data masking by the initial control and the secondary control, the percentage of unmasked records for each parameter at three data levels is shown in Table 5, and ~~T~~the effects of the two~~initial and secondary~~ controls are illustrated in Fig. 3 and described in detail below.

Table 5. Percentage of unmasked data for each parameter in each dataset.

| | SIGMA-A | | | SIGMA-B | | |
|---|---|---|---|---|---|---|
| | Level 1.1 | Level 1.2 | Level 1.3 | Level 1.1 | Level 1.2 | Level 1.3 |
| | % | % | % | % | % | % |
| $U_1$ | 98.0 | 98.0 | 92.1 | 99.7 | 99.7 | 97.7 |
| $WD_1$ | 98.0 | 96.7 | 91.8 | 99.7 | 99.2 | 97.2 |
| $T_1$ | 98.0 | 73.4 | 68.4 | 99.7 | 99.7 | 99.7 |
| $RH_1$ | 98.0 | 50.7 | 43.6 | 99.7 | 99.7 | 98.8 |
| $U_2$ | 98.0 | 98.0 | 94.1 | – | – | – |
| $WD_2$ | 98.0 | 97.1 | 93.8 | – | – | – |
| $T_2$ | 98.0 | 98.0 | 97.8 | – | – | – |
| $RH_2$ | 98.0 | 98.0 | 98.0 | – | – | – |
| $SW_d$ | 98.0 | 97.9 | 86.2 | 99.7 | 99.5 | 85.2 |
| $SW_u$ | 98.0 | 97.9 | 98.1 | 99.7 | 99.7 | 99.7 |
| $LW_d$ | 98.0 | 75.3 | 68.9 | 99.7 | 91.0 | 91.0 |
| $LW_u$ | 98.0 | 68.7 | 67.4 | 99.7 | 91.0 | 91.0 |
| $NIR_d$ | 98.0 | 97.9 | 86.6 | – | – | – |
| $NIR_u$ | 98.0 | 97.9 | 98.0 | – | – | – |
| $sh$ | 98.0 | 85.5 | 75.8 | 99.7 | 90.2 | 87.1 |
| $P_a$ | 98.0 | 97.9 | 97.9 | 99.7 | 99.7 | 99.7 |
| $st_1$ | 98.0 | 97.6 | 96.7 | – | – | – |
| $st_2$ | 98.0 | 97.9 | 97.3 | – | – | – |
| $st_3$ | 98.0 | 88.8 | 87.2 | – | – | – |
| $st_4$ | 98.0 | 97.0 | 96.2 | – | – | – |
| $st_5$ | 98.0 | 94.9 | 72.3 | – | – | – |
| $st_6$ | 98.0 | 95.2 | 56.7 | – | – | – |
| $\alpha_{sw}$ | – | – | 31.6 | – | – | 32.4 |
| $\alpha_{nir}$ | – | – | 33.5 | – | – | – |
| $st\_depth_1$ | – | – | 75.8 | – | – | – |
| $st\_depth_2$ | – | – | 75.8 | – | – | – |
| $st\_depth_3$ | – | – | 75.8 | – | – | – |
| $st\_depth_4$ | – | – | 75.8 | – | – | – |
| $st\_depth_5$ | – | – | 52.7 | – | – | – |
| $st\_depth_6$ | – | – | 36.9 | – | – | – |
| $SW_{d\_slope}$ | – | – | – | – | – | 83.7 |

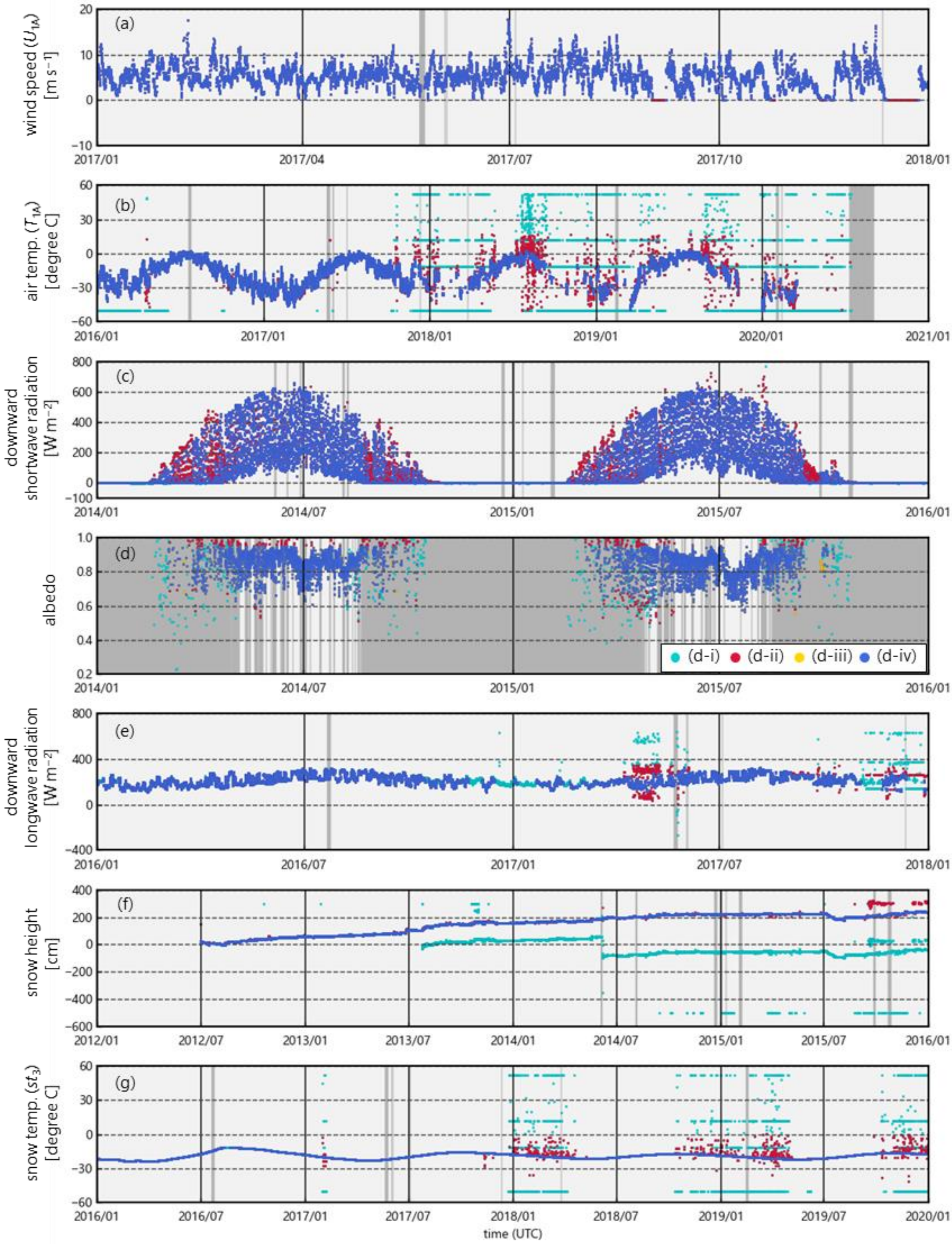
(a)
wind speed ($U_{1A}$) [m s⁻¹]
(b)
air temp. ($T_{1A}$) [degree C]
(c)
downward shortwave radiation [W m⁻²]
(d)
albedo
(d-i) (d-ii) (d-iii) (d-iv)
(e)
downward longwave radiation [W m⁻²]
(f)
snow height [cm]
(g)
snow temp. ($st_3$) [degree C]
time (UTC)

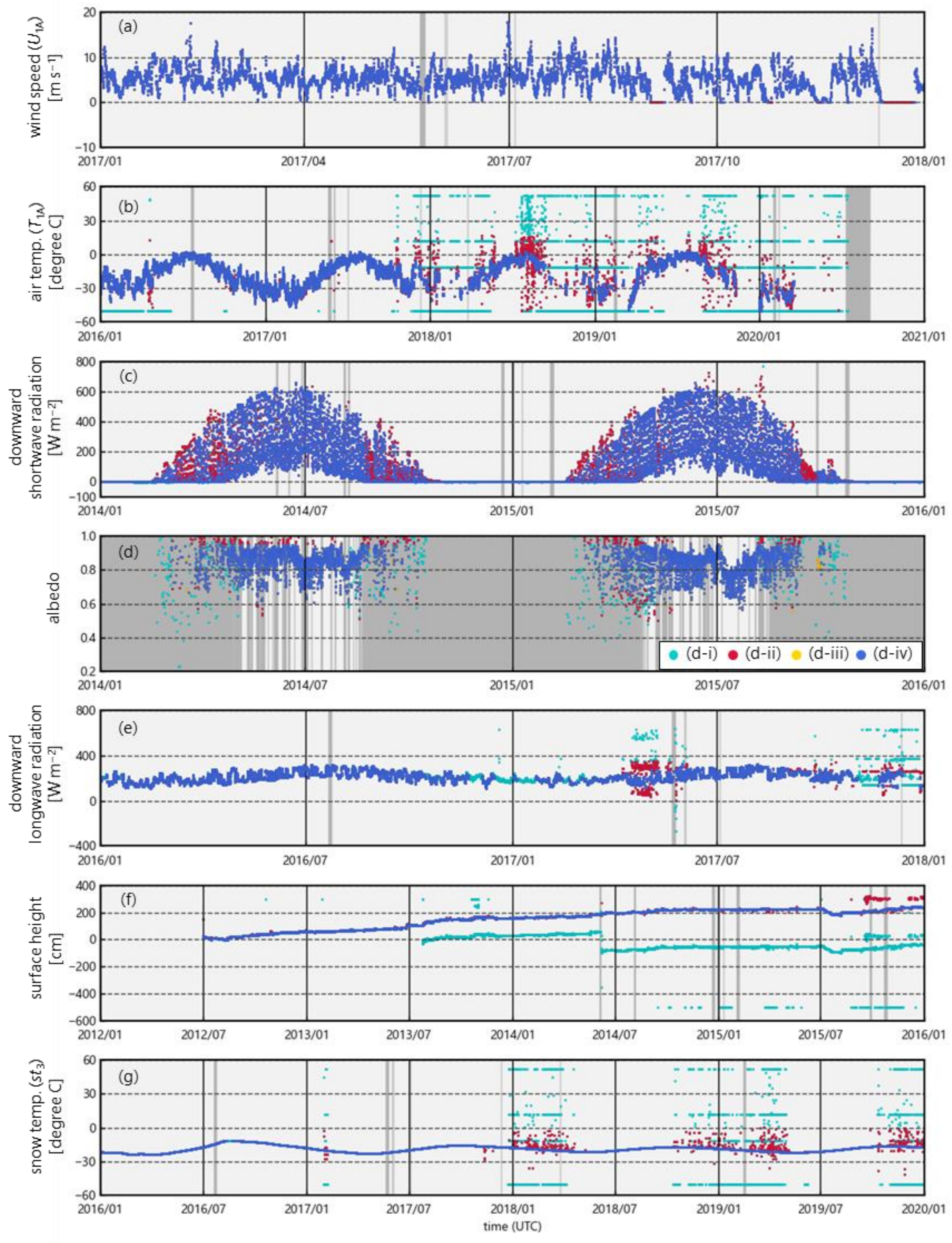


Figure 3. Examples of the initial and secondary controls for the SIGMA-A site: (a) wind speed ($U_{1A}$), (b) air temperature ($T_{1A}$), (c) downward shortwave radiation, (d) surface albedo, (e) downward longwave radiation, (f) ~~snow height~~surface height, and (g) snow temperature ($st_3$). In all panels except (d), the dark gray areas represent time periods in which data records in the Level 1.0 dataset were masked to produce the Level 1.1 dataset, light blue dots denote records masked by the initial control,

red dots denote records masked by the secondary control, and dark blue dots are the Level 1.3 data records. In panel (d), the gray shaded area represents the masked (−9999) data records that cannot be calculated due to the absence of, masked $SW_d$, or for other reasons. The light blue, red and yellow dots represent data points masked by three QC operations during the secondary control; see Sect. 4.2.4 for explanation.

#### 4.2.1. Wind speed and wind direction

When $U_n$ was zero for more than 6 continuous hours, $U_n$ and $WD_n$ were both flagged as erroneous (−9999) under the assumption that the wind sensor was blocked by snow and ice. Although the initial control eliminated no $U_n$ records, this step masked many values in the winter (Fig. 3a).

#### 4.2.2. Air temperature and relative humidity

Anomaly tests for air temperature and relative humidity were only applied to the lower-level sensor records for SIGMA-A (i.e., $T_{1A}$ and $RH_{1A}$). The anomaly test compared the difference ($\Delta T$ and $\Delta RH$) between readings of the upper and lower sensors (i.e., $|T_{1A} - T_{2A}|$ and $|RH_{1A} - RH_{2A}|$) to the respective medians and SDs of those parameters.~~:~~ The medians were calculated from the data before 1 September 2017, because the data after that date appeared to include many erroneous $T_{1A}$ records due to deterioration of the data logger or sensor. The SD criterion (γ in Procedure 2.0.1) was adjusted modestly (γ = 3) before 1 September, 2017 and more stringently (γ = 1) to detect outliers in the records of $T_{1A}$ and $RH_{1A}$ after the date, which were flagged as erroneous (−9999). The effectiveness of this adjustment is clear in Fig. 3b.

#### 4.2.3. Shortwave and near-infrared radiation

The anomaly test for shortwave and near-infrared radiation was intended to mask the noise resulting from a weak electric pulse at large solar zenith angles. The median and SD values were calculated from only the records ($SW_d$, $SW_u$, $NIR_d$, and $NIR_u$) at *solz* > 90.0° to distinguish this noise source according to P~~the~~ rocedure 2.0.1 for above parameters, where γ = 3. If the record deviates from its anomaly range, ~~following, using $SW_d$ as an example:~~

~~$SW_d$ < median_$SW_d$ + SD_$SW_d$ × 3. (2.3.1)~~

~~R~~the records ~~identified as noise~~ were identified as noise and modified to zero.

The downward radiation components were sometimes overestimated as a result of icing or riming over the glass dome of the pyranometer. To mask these erroneous values, we applied range tests based on $SW_{TOA}$ and ~~a~~ threshold values of atmospheric transmittance for each site $T_{rA}$ and $T_{rB}$ ($T_{rA}$ = 0.881 ~~for SIGMA-A~~ and $T_{rB}$ = 0.872 ~~for SIGMA-B~~) calculated by a radiative transfer model (Aoki et al., 1999, 2003) shown in Table 3~~:~~.

~~$SW_d < T_F\, SW_{TOA}$, (2.3.2)~~

~~$NIR_d < T_F\, f_{nir}\, SW_{TOA}$. (2.3.3)~~

Values of $SW_d$ and $NIR_d$ that were outside th~~is~~e range were flagged as erroneous (−9999).

To recognize other instances when the radiation sensor was covered with snow or frost, $SW_d$ and $NIR_d$ records corresponding to the following case that downward radiation is smaller than upward radiation was~~ere~~ flagged as erroneous (−9998), using $SW_\gamma$ as an example:

$SW_d$ ~~($NIR_d$)~~ $< SW_u$ ~~($NIR_u$)~~. (2.3.14)

Figure 3c shows that the initial control eliminated a few erroneous $SW_d$ data recorded in August 2015, whereas the secondary control masked many records, especially in February–May, that were affected by riming or frost.

#### 4.2.4. Shortwave and near-infrared albedo

We calculated albedos $\alpha_{sw}$ and $\alpha_{nir}$ from the $SW_d$ and $NIR_d$ datasets that were completed ~~had first undergone~~the secondary control. This calculation was done in four separate steps, shown by the color of dots in Fig. 3d.

(1) Flagging for low pyranometer sensitivity

At solar zenith angles near 90.0°, $SW_d$ and $NIR_d$ may not be an accurate measurement because of the low sensitivity of the pyranometer. We therefore masked $\alpha_{sw}$ and $\alpha_{nir}$ values at *solz* > 85.0° or when the $SW_d$ ($NIR_d$) value was below the median $SW_d$ ($NIR_d$) value for *solz* > 85.0°. Records masked in this step are shown in Fig. 3d as light blue dots (d-i).

(2) Range test for cold and warm periods

The range test used the upper and lower thresholds for $\alpha_{sw}$ and $\alpha_{nir}$ shown in Table 3, as determined by the radiative transfer calculation of Aoki et al. (2003, 2011) plus a small error margin. Those thresholds correspond to the assumed surface conditions during two parts of the year. For the cold period of October–April, we used the lower ~~following~~ thresholds for ~~different~~ dry snow at the SIGMA-A site ~~or~~and dry or wet snow~~ice~~ at the SIGMA-B site conditions.~~:~~

~~$0.6 < \alpha_{sw} < 0.95$ for dry snow at SIGMA-A, (2.4.1)~~

~~$0.5 < \alpha_{nir} < 0.90$ for dry snow at SIGMA-A, (2.4.2)~~

~~$0.4 < \alpha_{sw} < 0.95$ for dry or wet snow at SIGMA-B. (2.4.3)~~

For the warm period of May–September we used the ~~following~~ thresholds for wet snow at the SIGMA-A site and wet snow or dark ice at the SIGMA-B site conditions.~~:~~

~~$0.4 < \alpha_{sw} < 0.95$ for wet snow at SIGMA-A, (2.4.4)~~

~~$0.3 < \alpha_{nir} < 0.90$ for wet snow at SIGMA-A, (2.4.5)~~

~~$0.1 < \alpha_{sw} < 0.95$ for wet snow or dark ice at SIGMA-B. (2.4.6)~~

Records with albedo values beyond these theoretical thresholds were masked.

(3) Anomaly test in low atmospheric transmittance condition

The range test was augmented by an anomaly test to identify underestimates of $a_{sw}$ and $a_{nir}$ when $SW_d$ ($NIR_d$) was low and atmospheric transmittance ($t_r$) was small, typically at large solar zenith angles. ~~Whereas the first QC step in this phase used a criterion of *solz* > 85.0°, w~~We ~~relaxed it to *solz* > 80.0° and~~ masked $a_{sw}$ ($a_{nir}$) values that were unnaturally low owing to low $t_r$ and $SW_d$ ($NIR_d$) in *solz* > 80.0° condition. Data records that were masked in either the range or anomaly tests are shown in Fig. 3d as red dots (d-ii).

(4) Final steps

In cases where $LW_d$ was flagged as "−9998" during the initial control (see Sect. 4.1.4), $a_{sw}$ and $a_{nir}$ were flagged as "−9999" under the assumption that the radiation sensors were covered with snow or frost. The final step was a manual mask procedure. Data records that were masked in this phase are shown in Fig. 3d as orange dots (d-iii), and the final Level 1.3 dataset is displayed as blue dots (d-iv).

### 4.2.5. Longwave radiation

The anomaly test for $LW_d$ and $LW_u$ was conducted only for the SIGMA-A dataset using a standard longwave radiant flux ($LW_{std}$), a measure of the amount of longwave radiation from the near-surface atmosphere that was calculated from the air temperature measurement by Brock and Arnold (2000)

$$LW_{std} = \varepsilon^{*}\sigma(T_{2A} + 273.15)^{4}, \qquad \text{(xi)}$$

$$\varepsilon^{*} = (1 + \kappa n)\varepsilon_0, \qquad \text{(xii)}$$

$$\varepsilon_0 = 8.733 \times 10^{-3} \times (T_{2A} + 273.15)^{0.788}, \qquad \text{(xiii)}$$

where $\varepsilon^{*}$ is the atmospheric emissivity, $\sigma$ (= 5.670×10$^{-8}$) is the Stefan–Boltzmann constant, $\kappa$ (= 0.26) is a constant depending on cloud type (Braithwaite and Olsen, 1990), $n$ is the cloud cover amount ($n$: [0, 1] and set at 0.5 because it could not be determined), and $\varepsilon_0$ is the clear-sky emissivity. We assumed that $LW_{std}$ was a close approximation of the true longwave radiant fluxes and used the absolute difference between $LW_{std}$ and $LW_d$ or $LW_u$ (i.e., $\Delta LW_d$ or $\Delta LW_u$) and its median and SD as the basis of the anomaly test as following Procedure 2.0.1.

Because parts of the $LW_d$ dataset contained many erroneous records attributed to degradation of the data logger (see Fig. 3e), we reduced the SD criterion~~range limit~~ (γ = 1) in~~by half for two time periods,~~ 7 April to 7 June 2017 and after 1 September 2017. Except for those two periods, γ was set to "2" for both $\Delta LW_d$ and $\Delta LW_u$.~~The resulting criteria were~~

~~$\Delta LW_d$ < median_$\Delta LW_d$ + SD_$\Delta LW_d$ × 2 for all periods, except (2.5.1)~~

~~$\Delta LW_d$ < median_$\Delta LW_d$ + SD_$\Delta LW_d$ for two subperiods, (2.5.2)~~

~~$\Delta LW_u$ < median_$\Delta LW_u$ + SD_$\Delta LW_u$ × 2 for all periods. (2.5.3)~~

$LW_d$ and $LW_u$

r~~R~~ecords that were outliers under the~~se~~ criteria were flagged as erroneous (−9999). Figure 3e shows that the initial control (see Sect. 4.1.4) improved this anomaly test's efficacy, and the secondary control yielded a clean $LW_d$ time series.

### 4.2.6. ~~Snow height~~Surface height

The anomaly test for ~~snow height~~surface height masked data that displayed unrealistic fluctuations. Differences ($\Delta sh$) were determined with respect to mean and SD values from the preceding 72 h values during period 1, before 1 September 2017 ($sh_{mean1}$) and period 2, after 1 September 2017 ($sh_{mean2}$).~~ The difference between the two periods is that means were not calculated when the 72 h period included more than 48 flagged records in period 1 and more than 60 flagged records in period 2.~~ The $\Delta sh$ values were compared to the median plus SD of $\Delta sh$ for that period. In the period 1, the SD criterion in Procedure 2.0.1 was strict (γ = 1), and in the period 2, the criterion was relaxed (γ = 3). In addition, because ~~snow height~~surface height increased steadily in period 2, we derived the regression equation for this increase and identified outliers with respect to the SD of the regression, i.e. $\Delta sh_{reg}$ as follows:~~.~~ ~~The resulting criteria were~~

~~$\Delta sh_{mean1} < \mathrm{median}_1\_\Delta sh + \mathrm{SD}_1 \Delta sh,$ (2.6.1)~~

$$\Delta sh_{reg} < \mathrm{SD}_{reg}\_sh \quad \text{for after 1 September 2017.} \qquad (2.6.1)$$

~~$\Delta sh_{mean2} < \mathrm{median}_2\_\Delta sh + \mathrm{SD}_2 \Delta sh \times 3$ for after 1 September 2017. (2.6.3)~~

Records of $sh$ that varied beyond the anomaly ranges ~~se threshold values~~ were flagged as erroneous (−9999).

A manual mask procedure was added as a final step. The result of QC procedure is shown in Fig. 3f. The initial control, which corrected gaps resulting from the AWS maintenance (see Sect. 4.1.5), yielded the smoothed data record that enabled the application of the anomaly test. Sensor height dataset was made using initial sensor height (3 or 6 m) and the QC completed temporal surface height data. Therefore, QC for sensor height data has already been implemented through the QC for surface height data.

### 4.2.7. Snow temperature

In the first step, data records were masked when the snow temperature sensor was suspected to be located above the snow surface:

$$st\_depth_n < -1.0 \rightarrow st_n \ \text{flagged} -9999. \qquad (2.7.1)$$

where $st\_depth_n$ was calculated using ~~snow height~~surface height data and the initial setting depth of sensor "n" (see Sect. 3). The threshold of $st\_depth_n$ included a margin of 1.0 cm to reflect the accuracy of the ~~snow height~~surface height sensor. The $st_n$ was flagged as "−9997" if we could not judge whether the snow temperature sensor was located below the snow surface.

The anomaly test for $st_n$ consisted of two procedures. The first procedure relied on a temperature gap ($\Delta st_{d1}$) between $st_4$ and data from each of the other five levels ($st_{not4}$)~~,~~ (i.e., $\Delta st_{d1} =$

$|st_4 - st_{\text{not4}}|$), because $st_4$ had very few erroneous data. The SD criterion (γ) for this anomaly test was changed for each parameter depending on the variability of the data. ~~:~~

~~$|st_4 - st_{\text{not4}}| > \text{median\_}st_4 + \text{SD\_}st_{\text{not4}} \times y.$ (2.7.2)~~

~~where the multiplier $y$ is 1, 2, or 3 depending on the intensity of the anomaly variation, and determined based on the test results in each case.~~

The second procedure used the difference ($\Delta st_{d2}$) between $st_n$ and its mean value $st_{n\_mean}$ from the previous 72 h ($\Delta st_{d2} = |st_n - st_{n\_mean}|$), calculated using the same method as $sh_{mean}$ (see Sect. 4.2.6). The SD criteria (γ) were all unity in this test. ~~:~~

~~$|st_n - st_{n\_mean}| > \text{median\_}st_{n\_mean} + \text{SD\_}st_{n\_mean}.$ (2.7.3)~~

In both procedures, the median and SD terms were calculated from records for the full time period. Records detected as outliers were flagged as "−9999". Figure 3g shows the results of all procedures, using $st_3$ as an example.

#### 4.2.8. Atmospheric pressure

The time series of $P_a$ included only a few erroneous records. We masked outliers on the basis of

$$|P_a - P_{a\_mean}| > 20.0, \quad (2.8.1)$$

where $P_{a\_mean}$ is the average for the past 3 h (excluding masked data records). We set the threshold at 20.0, a higher value than the SD, because using the SD could have masked valid records.

## 5. Temporal variations of meteorological parameters

This section shows the results of simple analyses of the Level 1.3 dataset.

### 5.1. Air temperature and ~~snow height~~surface height

Figure 4 shows the air temperature fluctuations and ~~snow height~~surface height (*sh*) variations at both sites. Mean air temperatures (2013–2019) were −18.1 °C at the SIGMA-A site and −12.3 °C at the SIGMA-B site. The annual maxima were recorded every July at both sites, except for August 2019 at the SIGMA-B site. In contrast, the annual minima occurred in different months between December and March. The maximum was slightly positive at the SIGMA-A site, and it was above freezing in all years at the SIGMA-B site. Unusually high temperatures were recorded in mid-July 2015 (7.2 °C at SIGMA-A and 10.7 °C at SIGMA-B). Air temperatures exceeding 5.0 °C at SIGMA-A and 10.0 °C at SIGMA-B were common during that period.

~~Warm summers were observed at both sites in 2015, 2016, 2019, and 2020, as indicated by the cumulative positive degree-day (PDD) records in Fig. 5. PDD generally increased after mid-June and significantly ascended from late June to July. This tendency was especially strong in warmer years. PDDs were an order of magnitude greater at SIGMA-B than at SIGMA-A. They increased gradually~~

~~until late August at SIGMA-B, whereas the increases at SIGMA-A were stepwise and stopped earlier, in mid to late July.~~

~~Snow height~~Surface height steadily increased at the SIGMA-A site during the 8-year study period (Fig. 4), in which *sh* rose approximately 1 m in the mass-balance years (September to August) of 2013/14, 2016/17, and 2017/18, and decreased slightly in the summers of 2011/12, 2014/15, and 2019/20. Accumulations were notable in autumn and relatively small in winter. At the SIGMA-B site, in contrast, increases and decreases in *sh* were observed during each mass-balance year. Decreases in *sh* during summers were rare during the summers of 2012/13 and 2017/18 but common during the 2013/14, 2014/15, 2015/16, 2018/19, and 2019/20 summers, when decreases were greater than 1 m.

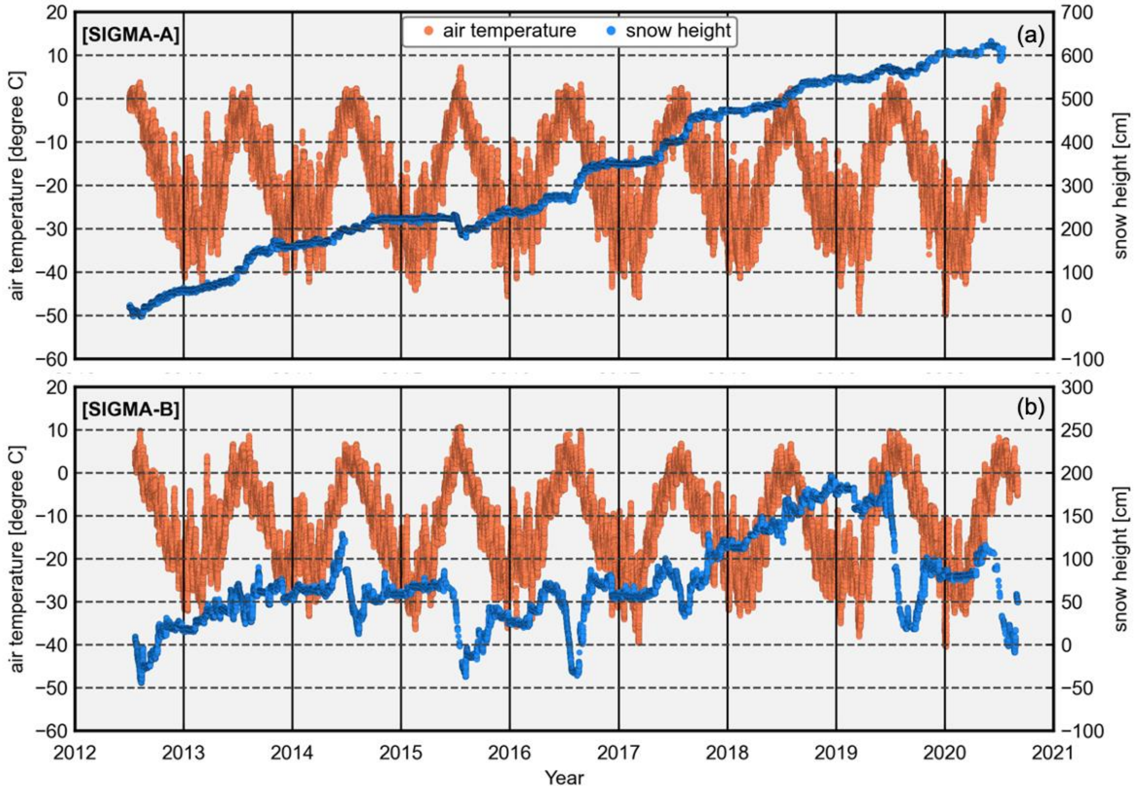

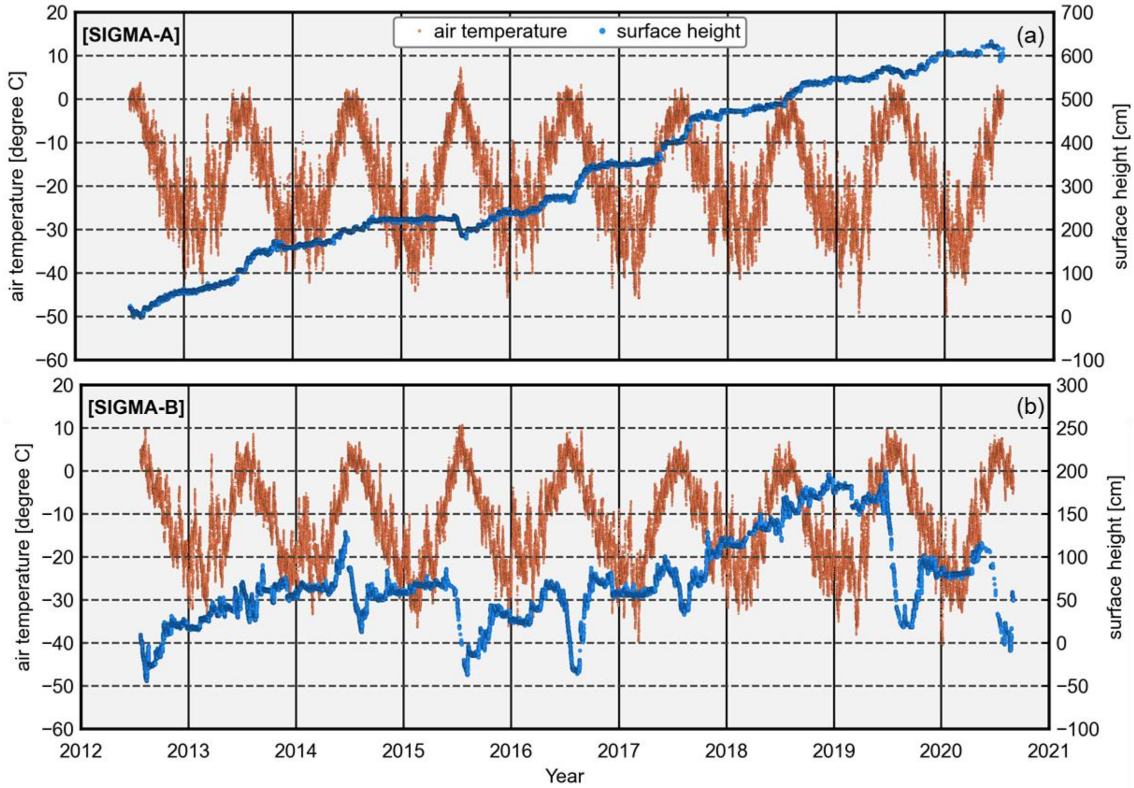


Figure 4. Time series of hourly air temperature and ~~snow height~~surface height at the (a) SIGMA-A (showing $T_2$ data) and (b) SIGMA-B sites.

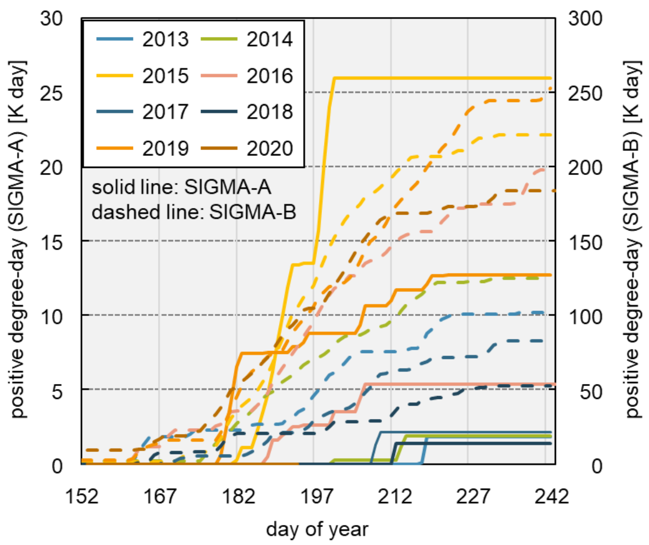


~~Figure 5. Cumulative positive degree-days at the SIGMA-A (solid lines) and SIGMA-B (dashed lines) sites from 1 June to 31 August, 2013–2020.~~

### 5.2. Atmospheric pressure and seasonal variation of temperature lapse rate

The time series of atmospheric pressure ($P_a$) at the SIGMA-A and SIGMA-B sites show a clear seasonal variation, high in summer and low in winter (Fig. 6). The two data records had similar variation patterns that were strongly correlated ($r = 0.98$). The mean values for the whole observation period were 833.1 hPa at site SIGMA-A and 894.2 hPa at site SIGMA-B (Table ~~3~~4). The difference in monthly mean $P_a$ between the sites was smaller in summer and larger in winter (Fig. 7a), and the amplitude of the annual cycle was greater at the SIGMA-A site.

~~The apparent lapse rate, indicated by the difference in monthly mean air temperatures between the elevations of the SIGMA-A and SIGMA-B sites, was approximately 8 K km$^{-1}$ in June and July and approximately 12 K km$^{-1}$ in November–February (Fig. 7b). Factors in summer that may contribute to this seasonal difference include a smaller difference in $P_a$ between the two sites and moister atmospheric conditions. The greater annual range of monthly air temperature at site SIGMA-A than at site SIGMA-B is likely also a winter effect. Winter is colder at SIGMA-A than at SIGMA-B because the SIGMA-A site is at a higher elevation and farther inland, where cooling by longwave emissions from the surface is greater and heat advection from the ocean is smaller. The temperature difference may lead in turn to a larger atmospheric pressure difference between the two sites in winter through its effect on atmospheric density. The combined summer and winter effects may be the reason that the apparent lapse rate is greater than the adiabatic reduction rate of the atmosphere (5 K for wet conditions and 10 K for dry conditions) (Fig. 7b).~~

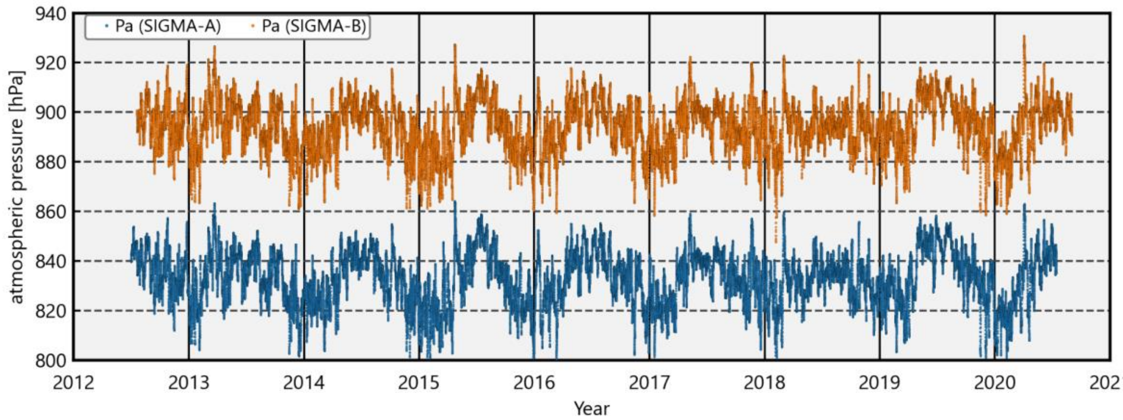


Figure 6. Time series of hourly atmospheric pressure ($P_a$) at the SIGMA-A and SIGMA-B sites.

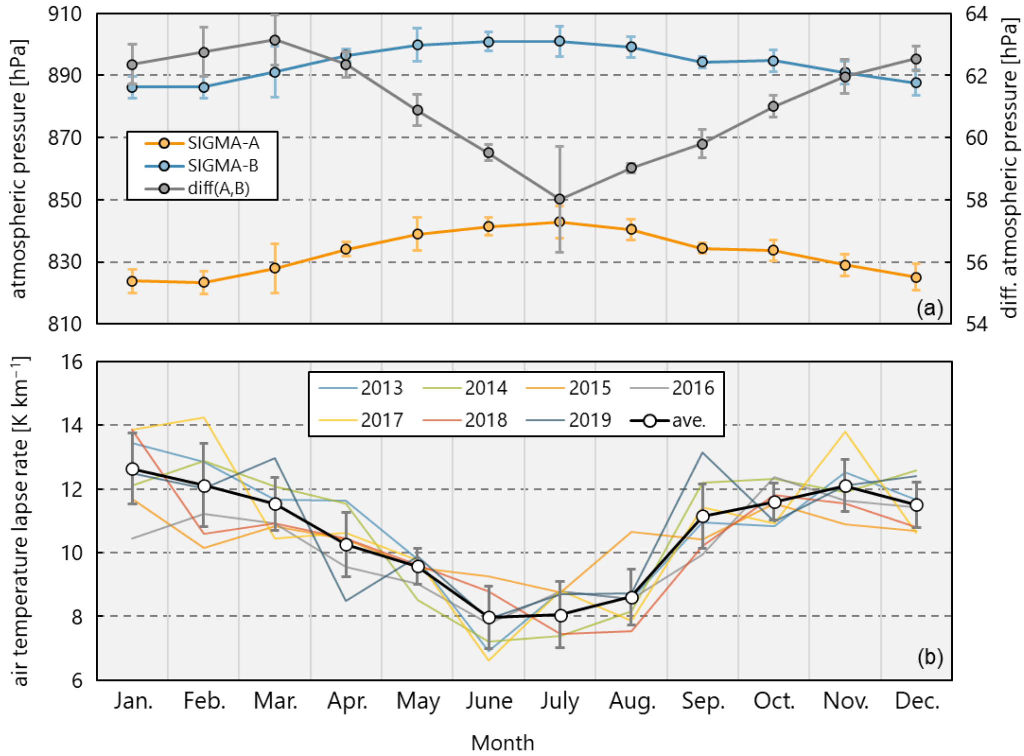


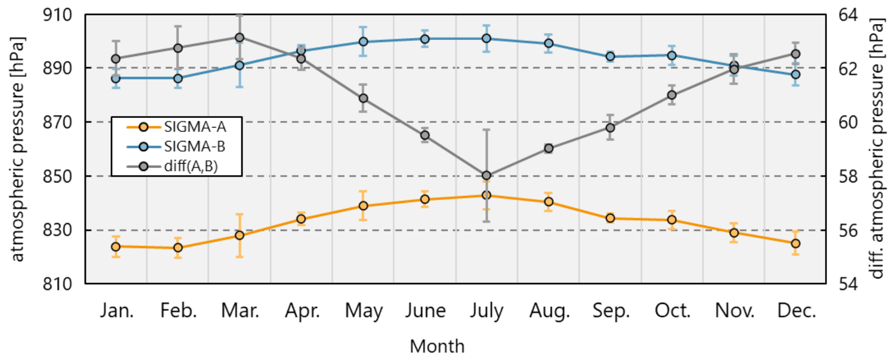


Figure 7. Time series of ~~(a)~~ ensemble averages of monthly mean atmospheric pressures during all years at both sites and their difference ~~and (b) monthly mean lapse rates of air temperature between the SIGMA-A and SIGMA-B sites for each year (colored lines) and their ensemble average during all years (open circles)~~. Error bars indicate ±1 SD.

### 5.3. Albedo

Whereas shortwave albedo ($a_{sw}$) was rarely lower than 0.7 at site SIGMA-A, near-infrared albedo ($a_{nir}$) was below 0.6 in 2012, 2015, 2016, 2019, and 2020 (Fig. 8). Because $a_{nir}$ depends on the snow grain size (Wiscombe and Warren, 1980), this finding implies that snow metamorphism progressed at the SIGMA-A site in those years (Hirose et al., 2021). A strong decrease in $a_{sw}$ was observed at the

SIGMA-B site during those same summers, which corresponded to notable decreases in ~~snow height~~surface height (Fig. 4b) and high PDDs (Fig. 5). The decreases in albedo may have accelerated snowmelt and caused the decreases in ~~snow height~~surface height at SIGMA-B during the warm summers of those years (see Sect. 5.1). It appears that the difference in albedo reduction between the SIGMA-A and SIGMA-B sites in summer originated from the difference in air temperature between the sites.

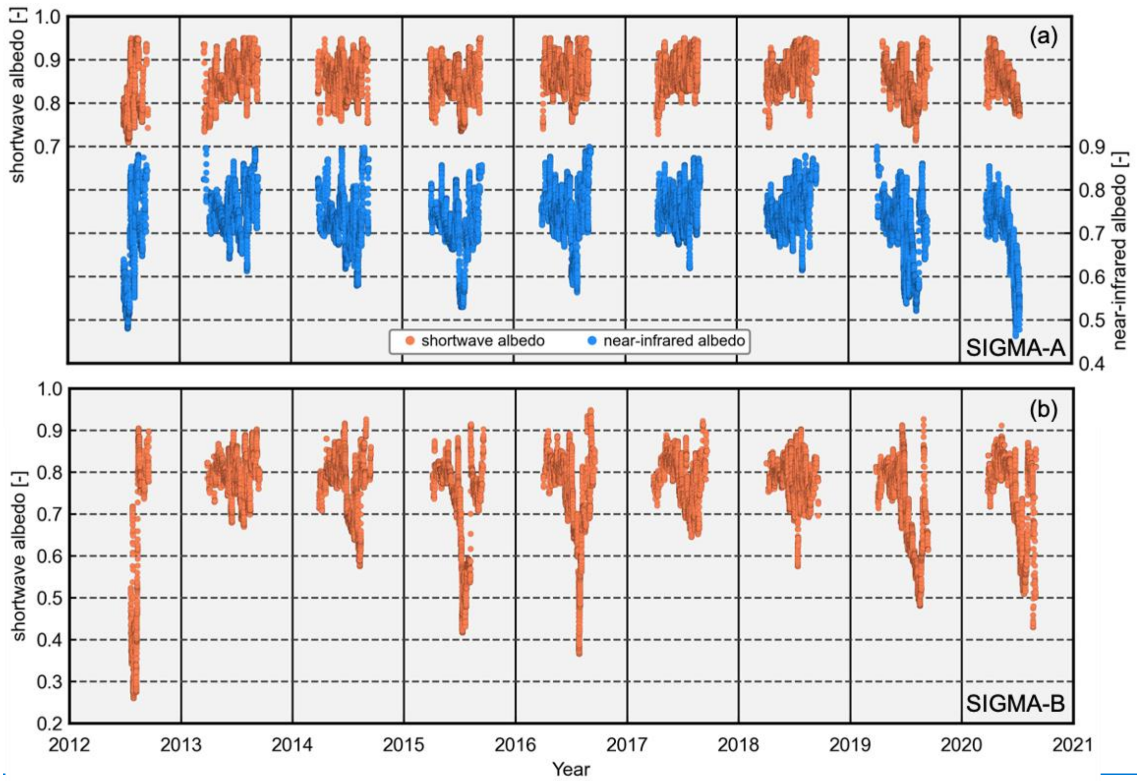

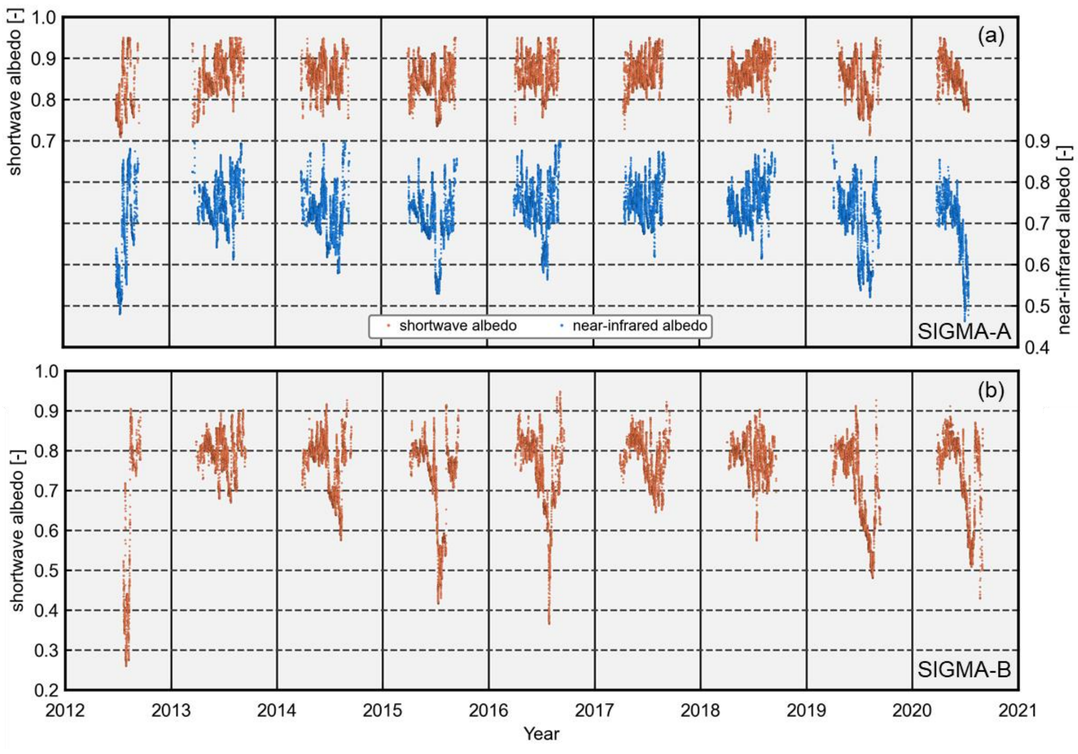


Figure 8. Time series of hourly shortwave and near-infrared albedos at the (a) SIGMA-A and (b) SIGMA-B sites.

**5.4. Snow temperature**

Figure 9 shows the time series of snow temperatures ($st_1$–$st_6$) and snow sensor depths ($st\_depth_{1-6}$). The sensor depths were calculated from each sensor's initial depths (see Sect. 3.1) and the ~~snow height~~surface height variations at the SIGMA-A site. Seasonal and short-term snow temperature fluctuations were observed, which became smaller after the 2016/17 winter season, when snow accumulation was very large (Fig. 4). We assumed that the sensors were buried more deeply at that time, resulting in smaller fluctuations in snow temperature. The annual mean snow temperatures after 2016, a year in which snow temperatures were relatively stable and less variable, were between −18.9 ± 0.5 °C ($st_4$) and −19.5 ± 1.7 °C ($st_5$).

Sensors recorded relatively high snow temperatures when they were positioned at shallow depths below the snow surface. However, in the summer of 2015, sensors $st_3$ and $st_4$ registered 0 °C even though they were more than 1 m below the snow surface. Air temperatures above freezing, and a large~~r~~ decrease in ~~snow height~~surface height were observed in this period (Figs. 4 and 5); thus, it is plausible that snowmelt occurred from the surface to depths near 120 cm, where $st_3$ was located at that time.

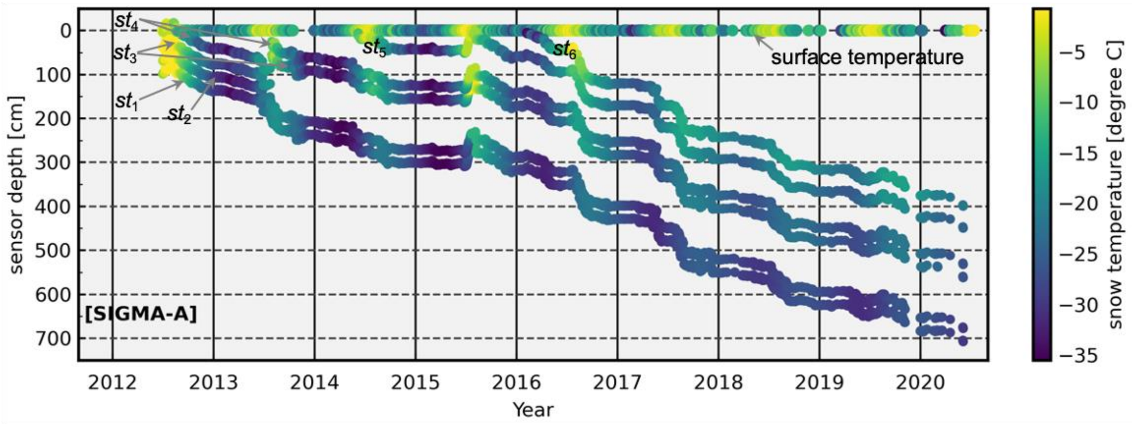


Figure 9. Time series of hourly snow temperatures ($st_1$–$st_6$), sensor depth, and surface temperature (calculated from upward longwave radiation) at the SIGMA-A site.

### 5.5. Longwave radiation

The occurrence frequency of longwave radiation, taken to represent the atmospheric condition, is often used as an indicator of climatological cloudiness (Stramler et al., 2011). Figure 10 shows the histograms of occurrence frequency of downward ($LW_d$) and net longwave radiation ($LW_{net} = LW_d - LW_u$) during July of all years at the SIGMA-A and SIGMA-B sites. The corresponding histograms for the four seasons (autumn: SON, winter: DJF, spring: MAM, summer: JJA) are shown in Figs. S1 and S2. The July $LW_d$ data from both sites had bimodal distributions, with a lower mode of 220–240 W m$^{-2}$ at SIGMA-A and 240–260 W m$^{-2}$ at SIGMA-B, and a higher mode of 290–310 W m$^{-2}$ at SIGMA-A and 310–330 W m$^{-2}$ at SIGMA-B. The histograms of July and seasonal $LW_{net}$ had similar but clearer bimodal distributions, with modes at approximately 0 W m$^{-2}$ and −70 W m$^{-2}$ (Figs. 10c-d and S2).

$LW_{net}$ can be regarded as an indicator of cloudiness, which can significantly change the downward longwave radiation and thus the surface temperature of the snow or ice. Both downward and net longwave radiation increase under overcast conditions because of blackbody radiation from the cloud cover that is absent in clear-sky conditions. Stramler et al. (2011) and Morrison et al. (2012) have argued that surface net longwave radiative flux has two modes in occurrence frequency (at −40 W m$^{-2}$ and 0 W m$^{-2}$), which correspond to clear-sky and overcast (low-level mixed-phase clouds) conditions. In overcast conditions, because the cloud base and the surface are in thermal equilibrium, the vertical thermal gradient is small and the longwave radiation budget is balanced ($LW_{net}$ = 0 W m$^{-2}$) at the surface. The two modes of $LW_{net}$ (0 W m$^{-2}$ and −70 W m$^{-2}$) at the two AWS sites appear to correspond to the modes proposed by these earlier studies.

The occurrence frequency of $LW_{net}$ in JJA appears to be more variable than those for the other seasons at both sites (Fig. S2). In these months, the air temperature rises and sea ice extent decreases, increasing the water vapor supply and advection from the surrounding sea to coastal Greenland (Kim and Kim, 2017; Liang et al., 2022). In such atmospheric conditions, the cloud formation process is susceptible to synoptic-scale disturbances. The histogram of $LW_{net}$ for July (Fig. 10) indicates clear-sky ($LW_{net} \cong -70$ W m$^{-2}$) in 2015, 2019, and 2020 and overcast conditions ($LW_{net} \cong 0$ W m$^{-2}$) in 2014 and 2018. In contrast, annual occurrence frequencies for SON and MAM were less variable than those for JJA. Overcast and clear-sky conditions dominated in SON and MAM, respectively. Our analysis shows that cloudiness in JJA was more variable than in other seasons, a result that is also borne out by satellite observations (Ryan et al., 2022).

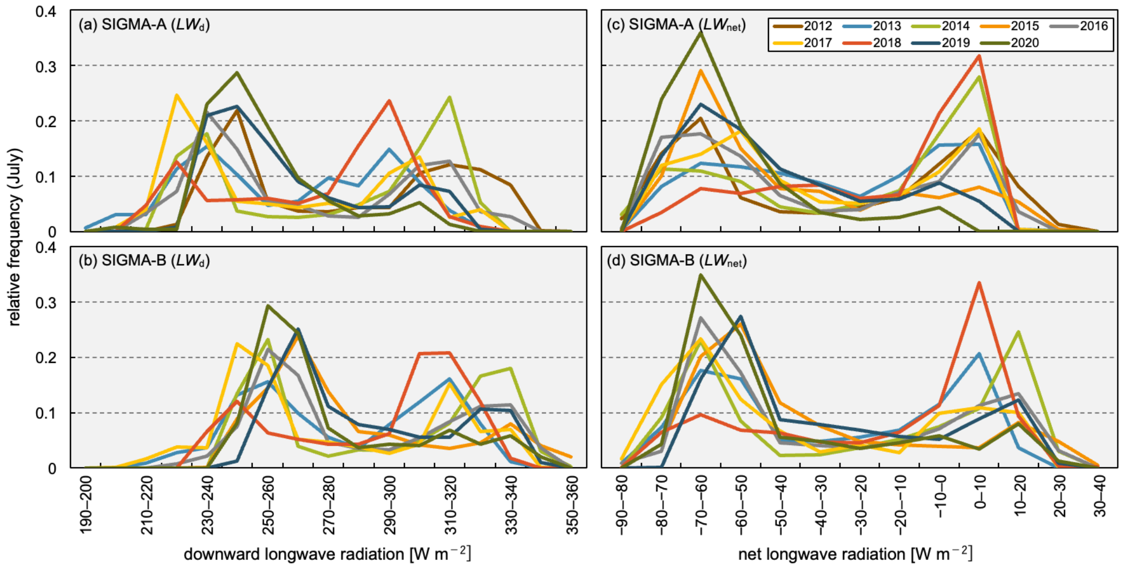


Figure 10. Histograms of the occurrence frequency of hourly downward longwave radiation ($LW_d$) and net longwave radiation ($LW_{net}$) observed at the SIGMA-A and SIGMA-B sites in July of all years in the study period. Each relative frequency represents the fraction of the total contained in each 10 W m$^{-2}$ bin.

## 6. Data availability

The Level 1.1, 1.2, and 1.3 datasets from this study are archived and available from the Arctic Data archive System (ADS) in the National Institute of Polar Research (Table 64), where they are stored in text (CSV) file format. Detailed information on the data content is presented in the file "data_format_*site-name*_*data-level*.csv" associated with each of these dataset files.

Table 64. Information for the archived datasets from the SIGMA-A and SIGMA-B sites.

| | |
|---|---|
| ***SIGMA-A*** | |
| Level 1.1 | |
| data name: | Quality-controlled datasets of Automatic Weather Station (AWS) at SIGMA-A site from 2012 to 2020: Level: 1.1 |
| file name: | SIGMA_AWS_SiteA_2012-2020_Lv1_1.csv |
| citation: | http://doi.org/10.17592/001.2022041301 |
| reference: | Nishimura et al. (2023a) |
| Level 1.2 | |
| data name: | Quality-controlled datasets of Automatic Weather Station (AWS) at SIGMA-A site from 2012 to 2020: Level: 1.2 |
| file name: | SIGMA_AWS_SiteA_2012-2020_Lv1_2.csv |
| citation: | http://doi.org/10.17592/001.2022041302 |
| reference: | Nishimura et al. (2023b) |
| Level 1.3 | |
| data name: | Quality-controlled datasets of Automatic Weather Station (AWS) at SIGMA-A site from 2012 to 2020: Level: 1.3 |
| file name: | SIGMA_AWS_SiteA_2012-2020_Lv1_3.csv |
| citation: | http://doi.org/10.17592/001.2022041303 |
| reference: | Nishimura et al. (2023c) |
| ***SIGMA-B*** | |
| Level 1.1 | |
| data name: | Quality-controlled datasets of Automatic Weather Station (AWS) at SIGMA-B site from 2012 to 2020: Level 1.1 |
| file name: | SIGMA_AWS_SiteB_2012-2020_Lv1_1.csv |
| citation: | http://doi.org/10.17592/001.2022041304 |
| reference: | Nishimura et al. (2023d) |
| Level 1.2 | |
| data name: | Quality-controlled datasets of Automatic Weather Station (AWS) at SIGMA-B site from 2012 to 2020: Level 1.2 |
| file name: | SIGMA_AWS_SiteB_2012-2020_Lv1_2.csv |
| citation: | http://doi.org/10.17592/001.2022041305 |
| reference: | Nishimura et al. (2023e) |
| Level 1.3 | |
| data name: | Quality-controlled datasets of Automatic Weather Station (AWS) at SIGMA-B site from 2012 to 2020: Level 1.3 |
| file name: | SIGMA_AWS_SiteB_2012-2020_Lv1_3.csv |
| citation: | http://doi.org/10.17592/001.2022041306 |
| reference: | Nishimura et al. (2023f) |

## 7. Summary and conclusion

This paper describes the in situ meteorological datasets from the SIGMA-A and SIGMA-B AWS sites in northwest Greenland and details the QC methods used in preparing the datasets. At this time when drastic environmental change is proceeding in the Arctic region, sound meteorological data and QC methods are of ever-growing importance.

The QC method offered here consists of two basic steps. The first step, the initial control, masks observations that are affected by mechanical malfunctions or local phenomena and is a pre-treatment for the second QC step. This step uses simple statistics to set the range of permissible variation in northwest Greenland for each observational parameter and flags erroneous records on the basis of that variation range. The second QC step, the secondary control, masks erroneous observations based on more stringent variation ranges as determined by the median and SD values of the full observation record. The QC procedures offered here may be valuable for scientists developing their own QC efforts.

We presented examples of time series of air temperature, ~~snow height~~surface height~~, PDD~~, atmospheric pressure, snow temperature, surface albedos, and longwave radiation based on the resulting hourly meteorological dataset for 2012–2020 in northwest Greenland. We also extracted information on climatological cloudiness based on $LW_{net}$ data derived from these in situ ground observations. Our primary findings are summarized in the following four points: (1) in the 2015 summer~~s of 2015, 2016, 2019, and 2020~~, high air temperature, in addition, 2016, 2019, 2020 summers ~~PDDs and~~ low surface albedos were recorded at both SIGMA-A and SIGMA-B sites. (2) Dramatic decreases in ~~snow height~~surface height occurred in 2015 at both AWS sites and in 2016, 2019, and 2020 at the SIGMA-B site. (3) Weather conditions in JJA were relatively variable in northwest Greenland compared to the other seasons. (4) Clear-sky conditions typified the summers of 2015, 2019, and 2020.

The datasets described here are archived in the open access Arctic Data archive System for all scientific communities. We anticipate that they will not only aid in understanding and monitoring the current climate in northwest Greenland but also contribute more broadly to the advancement of polar climate studies.

## Author contribution

All authors, excluding M. Nishimura, established the AWS systems and supported their maintenance. In addition, M. Nishimura developed and carried out the QC procedures and analyzed the observation data, TA designed and led the study project and provided technical support for the QC procedures, M. Niwano conducted pre-treatments for the meteorological data record and constructed a fundamental algorithm of the QC procedures, TY supported the field observations, especially logistical support, and KF provided advice on interpreting the observational data. All authors participated in the interpretation of results and gave final approval for publication.

## Competing interests

The authors declare that they have no conflict of interest.

## Acknowledgments

We recognize all members of the SIGMA project, the GRENE-Arctic Project in Greenland, and the Arctic Challenge for Sustainability II (ArCS II) project. We also thank all of those who supported the field observations. In particular, we thank Y. Iizuka (Hokkaido University), Y. Kurosaki (Hokkaido University), and A. Tsushima (Chiba University) for taking part in the field activities at the SIGMA-A site and establishing the AWS and Y. Komuro (National Institute of Polar Research) for technical advice. This study was conducted as a part of the "Snow Impurity and Glacial Microbe effects on abrupt warming in the Arctic (SIGMA)" Project supported by the Japan Society for the Promotion of Science Grant-in-Aid for Scientific Research numbers JP23221004 and JP16H01772, the Global Change Observation Mission-Climate (GCOM-C) research project of the Japan Aerospace Exploration Agency, and ArCS II Program Grant Number JPMXD1420318865. For the use of NunaGIS (http://en.nunagis.gl/) operated by Asiaq, Greenland Survey, in preparing Fig. 1, we acknowledge the National Snow and Ice Data Center's QGreenland package (Moon et al., 2021). The DEM data from Arctic DEMs were provided by the Polar Geospatial Center under NSF-OPP awards 1043681, 1559691, and 1542736.

## References

Aoki, T., Aoki, T., Fukabori, M., and Uchiyama, A.: Numerical simulation of the atmospheric effects on snow albedo with a multiple scattering radiative transfer model for the atmosphere-snow system, J. Meteorol. Soc. Japan, 77, 595-614, https://doi.org/10.2151/jmsj1965.77.2_595, 1999.

Aoki, T., Kuchiki, K., Niwano, M., Kodama, Y., Hosaka, M., and Tanaka, T.: Physically based snow albedo model for calculating broadband albedos and the solar heating profile in snowpack for general circulation models. J. Geophys. Res.: Atmos., 116 (D11114), 1–22. https://doi.org/10.1029/2010JD015507, 2011.

Aoki, T., Hachikubo, A., and Hori, M.: Effect of snow physical parameters on shortwave broadband albedos, J. Geophys. Res., 108, D19, 1–12. https://doi.org/10.1029/2003jd003506, 2003.

Aoki, T., Matoba, S., Uetake, J., Takeuchi, N., and Motoyama, H.: Field activities of the "Snow Impurity and Glacial Microbe effects on abrupt warming in the Arctic" (SIGMA) Project in Greenland in 2011-2013. Bull. Glaciol. Res., 32, 3–20. https://doi.org/10.5331/bgr.32.3, 2014.

Armstrong, R. L. and Brun, E. (Eds.).: Physical processes within the snow cover and their parameterization, in Snow and Climate: Physical Processes, Surface Energy Exchange and Modeling, Cambridge University Press, Cambridge N.Y., p. 58, 2008.

Behrens, K.: Radiation sensors, in: Springer handbook of atmospheric measurements, edited by: Foken, T., Springer International Publishing, pp. 297–357, https://doi.org/10.1007/978-3-030-52171-4_11, 2021.

Braithwaite, R. J. and Olesen, O. B.: A simple energy-balance model to calculate ice ablation at the margin of the Greenland ice sheet. J. Glaciol., 36, 222–228. https://doi.org/10.1017/S0022143000009473, 1990.

Brock, B. W. and Arnold, N. S.: A spreadsheet-based (Microsoft Excel) point surface energy balance model for glacier and snow melt studies. Earth Surf. Proc. Land., 25, 649–658. https://doi.org/10.1002/1096-9837(200006)25:6<649::AID-ESP97>3.0.CO;2-U, 2000.

Estévez, J., Gavilán, P., and Giráldez, J. V.: Guidelines on validation procedures for meteorological data from automatic weather stations, J. Hydrol., 402, 144–154. https://doi.org/10.1016/j.jhydrol.2011.02.031, 2011.

Fausto, R. S., van As, D., Mankoff, K. D., Vandecrux, B., Citterio, M., Ahlstrøm, A. P., Andersen, S. B., Colgan, W., Karlsson, N. B., Kjeldsen, K. K., Korsgaard, N. J., Larsen, S. H., Nielsen, S., Pedersen, A., Shields, C. L., Solgaard, A. M., and Box, J. E.: Programme for Monitoring of the Greenland Ice Sheet (PROMICE) automatic weather station data. Earth Syst. Sci. Data, 13, 3819–3845. https://doi.org/10.5194/essd-13-3819-2021, 2021.

~~Fettweis, X., Hofer, S., Krebs-Kanzow, U., Amory, C., Aoki, T., Berends, C., Born, A., Box, J., Delhasse, A., Fujita, K., Gierz, P., Goelzer, H., Hanna, E., Hashimoto, A., Huybrechts, P., Kapsch, M.-L., King, M., Kittel, C., Lang, C., L. Langen, P., T. M. Lenaerts, J., E. Liston, G., Lohmann, G., H. Mernild, S., Mikolajewicz, U., Modali, K., H. Mottram, R., Niwano, M., Noël, B., C. Ryan, J., Smith, A., Streffing, J., Tedesco, M., J. van de Berg, W., van den Broeke, M., S. W. van de Wal, R., van Kampenhout, L., Wilton, D., Wouters, B., Ziemen, F., and Zolles, T.: GrSMBMIP: Intercomparison of the modelled 1980–2012 surface mass balance over the Greenland Ice sheet, The Cryosphere, 1–35. https://doi.org/10.5194/tc-2019-321, 2020.~~

Fiebrich, C. A., Morgan, Y. R., McCombs, A. G., Hall, P. K., and McPherson, R. A.: Quality assurance procedures for mesoscale meteorological data. J. Atmos. Ocean. Tech., 27, 1565–1582. https://doi.org/10.1175/2010JTECHA1433.1, 2010.

Fröhlich, C.: Total solar irradiance observations. Surv. Geophys, 33, 453–473. https://doi.org/10.1007/s10712-011-9168-5, 2012.

Fujita, K., Matoba, S., Iizuka, Y., Takeuchi, N., Tsushima, A., Kurosaki, Y., and Aoki, T.: Physically based summer temperature reconstruction from melt layers in ice cores. Earth Space Sci., 8(e2020EA001590), 1–17. https://doi.org/10.1029/2020EA001590, 2021.

~~Hanna, E., Navarro, F. J., Pattyn, F., Domingues, C. M., Fettweis, X., Ivins, E. R., Nicholls, R. J., Ritz, C., Smith, B., Tulaczyk, S., Whitehouse, P. L., and Zwally, H. J.: Ice-sheet mass balance and climate change, Nature, 498, 51–59. https://doi.org/10.1038/nature12238, 2013.~~

Hirose, S., Aoki, T., Niwano, M., Matoba, S., Tanikawa T., Yamaguchi, S., , and Yamasaki, T.: Surface energy balance observed at the SIGMA-A site on the northwest Greenland ice sheet (in Japanese with English abstract). Seppyo, 83, 143–154, https://doi.org/10.5331/seppyo.83.2_143, 2021.

Hock, R. and Holmgren, B.: A distributed surface energy-balance model for complex topography and its application to Storglaciären, Sweden, J. Glaciol., 51, 25–36. https://doi.org/10.3189/172756505781829566, 2005.

~~IMBIE Team (Shepherd, A. et al.): Mass balance of the Greenland Ice Sheet from 1992 to 2018, Nature, 579, 233–239. https://doi.org/10.1038/s41586-019-1855-2, 2020.~~

IPCC: Summary for Policymakers. In: Climate Change 2021: The Physical Science Basis. Contribution of Working Group I to the Sixth Assessment Report of the Intergovernmental Panel on Climate Change [Masson-Delmotte, V., P. Zhai, A. Pirani, S. L. Connors, C. P an, S. Berger, N. Caud, Y. Chen, L. Goldfarb, M. I. Gomis, M. Huang, K. Leitzell, E. Lonnoy, J.B.R. Matthews, T. K. Maycock, T. Waterfield, O. Yeleki, R. Yu and B. Zhou (eds.)]. Cambridge University Press. In Press, 2021.

Jonsell, U., Hock, R., and Holmgren, B.: Spatial and temporal variations in albedo on Storglaciären, Sweden, J. Glaciol., 49, 59–68. https://doi.org/10.3189/172756503781830980, 2003.

Kim, H. M. and Kim, B. M.: Relative contributions of atmospheric energy transport and sea ice loss to the recent warm arctic winter. J. Clim., 30, 7441–7450. https://doi.org/10.1175/JCLI-D-17-0157.1, 2017.

Kurosaki, Y., Matoba, S., Iizuka, Y., Niwano, M., Tanikawa, T., Ando, T., Hori, A., Miyamoto, A., Fujita, S., and Aoki, T.: Reconstruction of sea ice concentration in northern Baffin Bay using deuterium excess in a coastal ice core from the north-western Greenland Ice Sheet. J. Geophys. Res. Atmos., 125. https://doi.org/10.1029/2019JD031668, 2020.

Liang, Y., Bi, H., Huang, H., Lei, R., Liang, X., Cheng, B., and Wang, Y.: Contribution of warm and moist atmospheric flow to a record minimum July sea ice extent of the Arctic in 2020. The Cryosphere, 16, 1107–1123. https://doi.org/10.5194/tc-16-1107-2022, 2022.

Makkonen, L. and Laakso, T.: Humidity measurements in cold and humid environments. Boundary-Layer Meteorol., 116, 131–147. https://doi.org/10.1007/s10546-004-7955-y, 2005.

Matoba, S., Niwano, M., Tanikawa, T., Iizuka, Y., Yamasaki, T., Kurosaki, Y., Aoki, T., Hashimoto, A., Hosaka, M., and Sugiyama, S.: Field activities at the SIGMA-A site, north-western Greenland Ice Sheet, 2017. Bull. Glaciol. Res., 36, 15–22. https://doi.org/10.5331/BGR.18R01, 2018.

Matoba, S., Yamaguchi, S., Tsushima, A., Aoki, T., and Sugiyama, S.: Surface mass balance variations in a maritime area of the north-western Greenland Ice Sheet (in Japanese with English abstract). Low Temperature Science, 75, 37–44, doi: 10.14943/lowtemsci.75.37, 2017.

Moon, T., Fisher, M., Harden, L., and Stafford, T.: QGreenland (v1.0.1) [software]. Available from https://qgreenland.org. https://doi.org/10.5281/zenodo.4558266, 2021.

Moradi, I.: Quality control of global solar radiation using sunshine duration hours, Energy, 34, 1–6. https://doi.org/10.1016/j.energy.2008.09.006, 2009.

Morino, S., Kurita, N., Hirasawa, N., Motoyama, H., Sugiura, K., Lazzara, M., Mikolajczyk, D., Welhouse, L., Keller, L., and Weidner, G.: Comparison of Ventilated and Unventilated Air Temperature Measurements in Inland Dronning Maud Land on the East Antarctic Plateau. J. Atmos. and Ocean. Technol., 38, 2061–2070. https://doi.org/10.1175/JTECH-D-21-0107.1, 2021.

Morrison, H., De Boer, G., Feingold, G., Harrington, J., Shupe, M. D., and Sulia, K.: Resilience of persistent Arctic mixed-phase clouds. Nat. Geosci., 5, 11–17. https://doi.org/10.1038/ngeo1332, 2012.

Mouginot, J., Rignot, E., Bjørk, A. A., van den Broeke, M., Millan, R., Morlighem, M., Noël, B., Scheuchl, B., and Wood, M.: Forty-six years of Greenland Ice Sheet mass balance from 1972 to 2018, P. Natl. Acad. Sci. USA, 116, 9239–9244. https://doi.org/10.1073/pnas.1904242116, 2019.

Nishimura, M., T. Aoki, M. Niwano, S. Matoba, T. Tanikawa, S. Yamaguchi, T. Yamasaki, A. Tsushima, K. Fujita, Y. Iizuka, Y. Kurosaki: Quality-controlled datasets of Automatic Weather Station (AWS) at SIGMA-A site from 2012 to 2020: Level 1.1, 1.00, Arctic Data archive System (ADS), Japan [dataset], http://doi.org/10.17592/001.2022041301, 2023a.

Nishimura, M., T. Aoki, M. Niwano, S. Matoba, T. Tanikawa, S. Yamaguchi, T. Yamasaki, A. Tsushima, K. Fujita, Y. Iizuka, Y. Kurosaki: Quality-controlled datasets of Automatic Weather Station (AWS) at SIGMA-A site from 2012 to 2020: Level 1.2, 1.20, Arctic Data archive System (ADS), Japan [dataset], http://doi.org/10.17592/001.2022041302, 2023b.

Nishimura, M., T. Aoki, M. Niwano, S. Matoba, T. Tanikawa, S. Yamaguchi, T. Yamasaki, A. Tsushima, K. Fujita, Y. Iizuka, Y. Kurosaki: Quality-controlled datasets of Automatic Weather Station (AWS) at SIGMA-A site from 2012 to 2020: Level 1.3, 1.20, Arctic Data archive System (ADS), Japan [dataset], http://doi.org/10.17592/001.2022041303, 2023c

Nishimura, M., T. Aoki, M. Niwano, S. Matoba, T. Tanikawa, S. Yamaguchi, T. Yamasaki, K. Fujita: Quality-controlled datasets of Automatic Weather Station (AWS) at SIGMA-B site from 2012 to 2020: Level 1.1, 1.00, Arctic Data archive System (ADS), Japan [dataset], http://doi.org/10.17592/001.2022041304, 2023d.

Nishimura, M., T. Aoki, M. Niwano, S. Matoba, T. Tanikawa, S. Yamaguchi, T. Yamasaki, K. Fujita: Quality-controlled datasets of Automatic Weather Station (AWS) at SIGMA-B site from 2012 to 2020: Level 1.2, 1.10, Arctic Data archive System (ADS), Japan [dataset], http://doi.org/10.17592/001.2022041305, 2023e.

Nishimura, M., T. Aoki, M. Niwano, S. Matoba, T. Tanikawa, S. Yamaguchi, T. Yamasaki, K. Fujita: Quality-controlled datasets of Automatic Weather Station (AWS) at SIGMA-B site from 2012 to 2020: Level 1.3, 1.20, Arctic Data archive System (ADS), Japan [dataset], http://doi.org/10.17592/001.2022041306, 2023f.

Niwano, M., Aoki, T., Matoba, S., Yamaguchi, S., Tanikawa, T., Kuchiki, K., and Motoyama, H.: Numerical simulation of extreme snowmelt observed at the SIGMA-A site, northwest Greenland, during summer 2012. The Cryosphere, 9, 971–988. https://doi.org/10.5194/tc-9-971-2015, 2015.

Niwano, M., Aoki, T., Hashimoto, A., Matoba, S., Yamaguchi, S., Tanikawa, T., Fujita, K., Tsushima, A., Iizuka, Y., Shimada, R., and Hori, M.: NHM-SMAP: Spatially and temporally high-resolution nonhydrostatic atmospheric model coupled with detailed snow process model for Greenland Ice

Sheet. The Cryosphere, 12, 635–655. https://doi.org/10.5194/tc-12-635-2018, 2018.

~~Niwano, M., Aoki, T., Hashimoto, A., Matoba, S., Yamaguchi, S., Tanikawa, T., Fujita, K., Tsushima, A., Iizuka, Y., Shimada, R., and Hori, M.: NHM-SMAP: Spatially and temporally high-resolution nonhydrostatic atmospheric model coupled with detailed snow process model for Greenland Ice Sheet. The Cryosphere, 12, 635–655. https://doi.org/10.5194/tc-12-635-2018, 2018.~~

Niwano, M., Box, J. E., Wehrlé, A., Vandecrux, B., Colgan, W. T., and Cappelen, J.: Rainfall on the Greenland Ice Sheet: Present-day climatology from a high-resolution non-hydrostatic polar regional climate model. Geophys. Res. Lett., 48(e2021GL092942), 1–11. https://doi.org/10.1029/2021GL092942, 2021.

Noël, B., van de Berg, W. J., Lhermitte, S., and van den Broeke, M. R.: Rapid ablation zone expansion amplifies north Greenland mass loss, Sci. Adv., 5, 2–11. https://doi.org/10.1126/sciadv.aaw0123, 2019.

Onuma, Y., Takeuchi, N., Tanaka, S., Nagatsuka, N., Niwano, M., and Aoki, T.: Observations and modelling of algal growth on a snowpack in north-western Greenland. The Cryosphere, 12, 2147–2158. https://doi.org/10.5194/tc-12-2147-2018, 2018.

Porter, C., Morin, P., Howat, I., Noh, M. J., Bates, B., Peterman, K., Keesey, S., Schlenk, M., Gardiner, J., Tomko, K., Willis, M., Kelleher, C., Cloutier, M., Husby, E., Foga, S., Nakamura, H., Platson, M., Wethington, M. Jr., Williamson, C., Bauer, G., Enos, J., Arnold, G., Kramer, W., Becker, P., Doshi, A., D'Souza, C., Cummens, P., Laurier, F., Bojesen, M.: "ArcticDEM", https://doi.org/10.7910/DVN/OHHUKH, Harvard Dataverse, V1, [Accessed in January 18, 2022], 2018.

Rottman, G.: Measurement of total and spectral solar irradiance. Space Sci. Rev., 125, 39–51. https://doi.org/10.1007/s11214-006-9045-6, 2006.

Ryan, J. C., Smith, L. C., Cooley, S. W., Pearson, B., Wever, N., Keenan, E., and Lenaerts, J. T. M.: Decreasing surface albedo signifies a growing importance of clouds for Greenland Ice Sheet meltwater production. Nat. Comm., 13(4205), 1–8. https://doi.org/10.1038/s41467-022-31434-w, 2022.

~~Shimada, R., Takeuchi, N., and Aoki, T.: Inter-annual and geographical variations in the extent of bare ice and dark ice on the Greenland ice sheet derived from MODIS satellite images. Front. Earth Sci., 4:43, 1–10. https://doi.org/10.3389/feart.2016.00043, 2016.~~

Steffen, C. and Box, J. E.: Surface climatology of the Greenland ice sheet: Greenland Climate Network 1995-1999, J. Geophys. Res., 106, D24, 33951–33964, 2001.

Stramler, K., Del Genio, A. D., and Rossow, W. B.: Synoptically driven Arctic winter states. J. Clim., 24, 1747–1762. https://doi.org/10.1175/2010JCLI3817.1, 2011.

Sugiyama, S., Sakakibara, D., Matsuno, S., Yamaguchi, S., Matoba, S., and Aoki, T.: Initial field observations on Qaanaaq ice cap, north-western Greenland, Ann. Glaciol., 55, 25–33.

https://doi.org/10.3189/2014AoG66A102, 2014.

Takeuchi, N., Sakaki, R., Uetake, J., Nagatsuka, N., Shimada, R., Niwano, M., and Aoki, T.: Temporal variations of cryoconite holes and cryoconite coverage on the ablation ice surface of Qaanaaq Glacier in northwest Greenland. Ann. Glaciol., 59, 21–30. https://doi.org/10.1017/aog.2018.19, 2018.

Tanikawa, T., Hori, M., Aoki, T., Hachikubo, A., Kuchiki, K., Niwano, M., Matoba, S., Yamaguchi, S., and Stamnes, K.: In situ measurements of polarization properties of snow surface under the Brewster geometry in Hokkaido, Japan, and northwest Greenland ice sheet. J. Geophys. Res., 119, 13,946-13,964. https://doi.org/10.1002/2014JD022325, 2014.

Tsutaki, S., Sugiyama, S., Sakakibara, D., Aoki, T., and Niwano, M.: Surface mass balance, ice velocity and near-surface ice temperature on Qaanaaq Ice Cap, north-western Greenland, from 2012 to 2016, Ann. Glaciol., 58, 181–192. https://doi.org/10.1017/aog.2017.7, 2017.

van As, D., Fausto, R. S., Ahlstrøm, A. P., Andersen, S. B., Andersen, M. L., Citterio, M., Edelvang, K., Gravesen, P., Machguth, H., Nick, F. M., Nielsen, S., and Anker, W.: Programme for Monitoring of the Greenland Ice Sheet (PROMICE): First temperature and ablation records, Geol. Surv. Den. Greenl., 23, 73–76. https://doi.org/10.34194/geusb.v23.4876, 2011.

van den Broeke, M., van As, D., Reijmer, C., and van de Wal, R.: Assessing and improving the quality of unattended radiation observations in Antarctica, J. Atmos. Ocean. Tech., 21, 1417–1431. https://doi.org/10.1175/1520-0426(2004)021<1417:AAITQO>2.0.CO;2, 2004a.

van den Broeke, M., Reijmer, C., and van de Wal, R.: Surface radiation balance in Antarctica as measured with automatic weather stations, J. Geophys. Res., 109, D09103, 1–17. https://doi.org/10.1029/2003JD004394, 2004b.

van de Wal, R. S. W., Greuell, W., Van den Broeke, M. R., Reijmer, C. J., and Oerlemans, J.: Surface mass-balance observations and automatic weather station data along a transect near Kangerlussuaq, West Greenland. Ann. Glaciol., 42, 311–316. https://doi.org/10.3189/172756405781812529, 2005.

Wehrli, C.: World Radiation Center (WRC) Publication. Davos-Dorf, Switzerland, 615, pp. 10-17, 1985.

Wiscombe, W. J., and Warren S. G.: A model for the spectral albedo of snow. I, Pure snow. J. Atmos. Sci., 37, 2712–2733., 1980.

Yamaguchi, S., Matoba, S., Yamazaki, T., Tsushima, A., Niwano, M., Tanikawa, T., and Aoki, T.: Glaciological observations in 2012 and 2013 at SIGMA-A site, Northwest Greenland. Bull. Glaciol. Res., 32, 95–105. https://doi.org/10.5331/bgr.32.95, 2014.